Temperature-Dependent Surface Anisotropy in (110) Epitaxial Rare Earth Iron Garnet Films

Yixuan Song, Katharina Lasinger, Hao Tang, Ju Li, Geoffrey S. D. Beach,* and Caroline A. Ross*

Ferrimagnetic oxide thin films are important material platforms for spintronic devices. Films grown on low symmetry orientations such as (110) exhibit complex anisotropy landscapes that can provide insight into novel phenomena such as spin-torque auto-oscillation and spin superfluidity. Using spin-Hall magnetoresistance measurements, the in-plane (IP) and out-of-plane (OOP) uniaxial anisotropy energies are determined for a thickness series (5–50 nm) of europium iron garnet (EuIG) and thulium iron garnet (TmIG) films epitaxially grown on a gadolinium gallium substrate with (110) orientation and capped with Pt. Pt/EuIG/GGG exhibits an (001) easy plane of magnetization perpendicular to the substrate, whereas Pt/TmIG/GGG exhibits an (001) hard plane of magnetization perpendicular to the substrate with an IP easy axis. Both IP and OOP surface anisotropy energies comparable in magnitude to the bulk anisotropy are observed. The temperature dependence of the surface anisotropies is consistent with first-order predictions of a simplified Néel surface anisotropy model. By taking advantage of the thickness and temperature dependence demonstrated in these ferrimagnetic oxides grown on the low symmetry (110) orientations, the complex anisotropy landscapes can be tuned to act as a platform to explore rich spin textures and dynamics.

Y. Song, K. Lasinger, H. Tang, J. Li, G. S. D. Beach, C. A. Ross
Department of Materials Science and Engineering
Massachusetts Institute of Technology
Cambridge, Massachusetts 02139, USA
E-mail: gbeach@mit.edu; caross@mit.edu
K. Lasinger
Department of Materials
ETH Zurich
Zurich CH-8093, Switzerland
J. Li
Department of Nuclear Science and Engineering
Massachusetts Institute of Technology
Cambridge, Massachusetts 02139, USA

1. Introduction

Magnetic thin films and heterostructures are important material platforms for a range of technological applications including magnetic tunnel junctions in magnetic random-access memory,[1,2] spin-torque oscillators,[3] racetrack memory,[4] magnonic devices,[5] and more. Recently, oxide-based spintronics has raised interest with recent developments focusing on ferrimagnetic and antiferromagnetic oxides and multiferroics.[6–13] Iron garnets (IGs, $R_3Fe_5O_{12}$ where R is a lanthanide, Y or Bi) are ferrimagnetic oxides that show the potential benefits of ultra-fast dynamics for fast current-driven and optical switching,[9] low damping for efficient magnon propagation,[10,11] and reduced power consumption because of current confinement within the charge-to-spin conversion layer. Further, the spin-orbit coupling (SOC) in rare earth IGs (REIGs) also offers opportunities to explore exotic physical phenomena including antisymmetric exchange interaction,[12] chiral spin textures,[13] and orbital current transport and switching.[14] Demonstrating these promising functionalities in REIGs relies on the engineering of appropriate anisotropy landscapes which vary significantly with the choice of rare-earth (including Y) and other elements such as Bi. Perpendicular magnetic anisotropy achieved through strain engineering in epitaxial films of europium iron garnet ($Eu_3Fe_5O_{12}$ or EuIG), thulium iron garnet ($Tm_3Fe_5O_{12}$ or TmIG), terbium iron garnet ($Tb_3Fe_5O_{12}$ or TbIG), and Bi-substituted yttrium iron garnet ($Y_3Fe_5O_{12}$ or YIG)[15–17] allowed for the demonstration of spin-orbit torque (SOT) switching,[18] the study of interfacial Dzyaloshinskii-Moriya interaction (DMI),[12] and SOT-driven domain wall motion.[19]

Epitaxial thin film growth techniques allow precise control and engineering of crystal symmetry. While films are conventionally grown on substrate crystal orientations with high symmetry such as C_4 on (100) or C_3 on (111) to obtain isotropic electronic, magnetic, and optical properties within the film plane,[20] films with low crystal symmetry have raised interest. A lower crystal symmetry, C_2 on (110), has been predicted and demonstrated to be an essential criterion for a wide range of novel spin textures and spin dynamics. For example, antiskyrmions

**ADVANCED
SCIENCE NEWS**

www.advancedsciencenews.com

**NANO · MICRO
small**

www.small-journal.com

rely on anisotropic DMI,[21] and spin-torque auto-oscillation and spin superfluidity require systems with vertical easy-plane anisotropy.[22–25] The SOT switching of in-plane (IP) magnetization, which provides a field-free alternative to the SOT switching of perpendicular magnetization,[26] also requires an IP symmetry breaking (C_2) to stabilize distinct IP states.

Oxide surfaces and interfaces play a critical role in controlling the properties of epitaxial thin films since the total film thickness is typically only at the nanometer scale. Atoms at surfaces and interfaces experience a bonding environment different from the bulk. Consequently, surfaces and interfaces exhibit distinct structural, chemical, electronic, and magnetic properties when compared to the bulk material.[27,28] In the realm of magnetic materials, magnetic anisotropy is a crucial physical property that dictates the magnetization orientation at equilibrium, the dynamic response, and the critical length scales of magnetic textures. Due to inversion symmetry breaking at surfaces and interfaces, the surface layer of atoms can contribute to an additional magnetic anisotropy, termed magnetic surface anisotropy.[29] While this contribution to anisotropy has been well studied for high symmetry orientations,[30–35] oxide surfaces on the low symmetry (110) orientation remain poorly explored.

Here, using spin-Hall magnetoresistance (SMR) measurements, we compare the thickness dependence of the anisotropy energy for EuIG, TmIG, and YIG epitaxially grown on the (110) orientation of gadolinium gallium garnet substrates ($Gd_3Ga_5O_{12}$ or GGG) by pulsed laser deposition (PLD) and capped with Pt. The rare-earth ions Eu^{3+}, Tm^{3+}, and Y^{3+} correspond to a strong SOC with a large magnetoelastic coefficient, a strong SOC with a small magnetoelastic coefficient, and a weak SOC with a small magnetoelastic coefficient, respectively.[36] These three rare-earth substitutions form an informative dataset for comparison. In both EuIG and TmIG films, we observed a strong IP surface anisotropy, comparable in magnitude to the bulk anisotropy energies, while a negligible IP surface and bulk anisotropy was present in YIG films. With density functional theory (DFT) calculations, we determined the atomic configurations for the lowest energy surface, which shows a C_2 symmetry. This symmetry allows both an IP and an out-of-plane (OOP) surface anisotropy contribution, denoted as $K_{IP, surface}$ and $K_{OOP, surface}$, respectively. A set of temperature-dependent measurements shows that both the surface and bulk anisotropy contributions decrease with increasing temperature, consistent with the Néel surface anisotropy model. The demonstration of complex anisotropy landscapes tunable by film thickness and temperature provides an important stepping-stone for spintronic device engineering and spin dynamics investigations.

2. Surface Anisotropy Model

In Néel's surface anisotropy model,[29] missing bonds and therefore magnetic pair interaction terms at the surface naturally give rise to a layer of atoms that contribute to a total anisotropy energy differently from those in the bulk. The magnetic pair interaction energy between atoms $w(r, \psi)$ is expanded in Legendre polynomials:[29,32]

$$w(r, \psi) = G(r) + L(r)\left(\cos^2\psi - \frac{1}{3}\right)$$
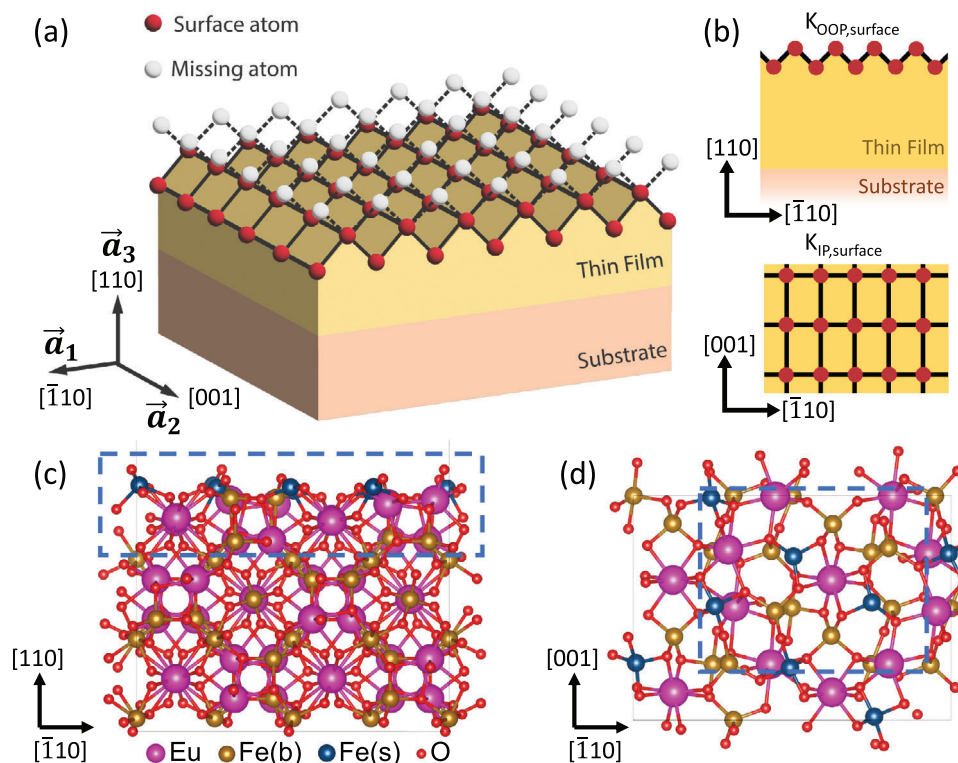$$+ Q(r)\left(\cos^4\psi - 6/7\cos^2\psi - 3/35\right) + \cdots \quad (1)$$

The interaction energy depends on ψ, the angle between the bond axis and the magnetization vector $\boldsymbol{M}$, and on the distance between the pair of atoms r. The first term is spatially isotropic, e.g. magnetic exchange $E_{ex} = -J_{ij}S_i \cdot S_j$ and does not contribute to the anisotropy. The second, dipolar term describes anisotropies with a twofold symmetry. The third, quadrupolar term describes anisotropies of cubic symmetry. The dipolar term typically dominates over the quadrupolar term. The magnetic anisotropy of a single crystal film can then be calculated by summing up this interaction energy for all nearest-neighbor pairs of atoms in the film.

Strain can be present in an epitaxial thin film because of the lattice mismatch between the film and the substrate. We consider a coordinate system with $\boldsymbol{a}_1$ and $\boldsymbol{a}_2$ describing the direction vectors within the film plane and $\boldsymbol{a}_3$ is the film normal. With the strain tensor defined in Equation. (2), where a uniform strain of $e_0 = (a_{substrate} - a_{film})/a_{film}$ within the film is assumed, and ν denotes the Poisson ratio, the strained bond length and bond axis can be calculated and propagated into the interaction energy. The coefficient for the dipolar term in Equation (1) can be approximated with the first-order Taylor's expansion of $L(r)$ about the unstrained bond length $L(r) = L(r_0) + (\vec{r}_0 \cdot e \cdot \vec{r}_0)\frac{dL}{dr}|_{r_0}$.

$$e = \begin{pmatrix} e_{11} & e_{12} & e_{13} \\ e_{21} & e_{22} & e_{23} \\ e_{31} & e_{32} & e_{33} \end{pmatrix} = e_0 \begin{pmatrix} 1 & 0 & 0 \\ 0 & 1 & 0 \\ 0 & 0 & \frac{-2\nu}{1-\nu} \end{pmatrix} \quad (2)$$

Symmetry arguments show that a threefold or higher rotation axis is required to ensure isotropic properties in the plane normal to that axis.[20] Conversely, the symmetry at the surface of a (110) film plane in a cubic structure reduces to C_{2v}. The symmetry breaking, illustrated with the ball and stick model in **Figure 1a,b** is essential to give rise to both an IP and OOP surface anisotropy in a system with a cubic structure. An OOP surface anisotropy contribution arises from the inversion symmetry breaking at the surface and an IP surface anisotropy contribution arises from the asymmetry between [001] and [$\bar{1}$10] directions on a (110) surface. Analysis using Néel's surface anisotropy approach quantifies the surface contribution to both IP and OOP anisotropy, represented by $K_{IP, surface}$ and $K_{OOP, surface}$, respectively.[32,33] This was also confirmed in experiments.[34] The IP anisotropy $K_{IP, surface}$ is expected to be large due to the presence of a zeroth order $L(r_0)$ term, which for a centrosymmetric system is compensated in the bulk. For a (110) film the surface anisotropy can be written as Equation (3), with the coordinate system being defined as $\boldsymbol{a}_1 = [\bar{1}10]$, $\boldsymbol{a}_2 = [001]$ and $\boldsymbol{a}_3 = [110]$:

$$K_{110, surface} = \left(\frac{1}{2}L(r_0) - e_0 L(r_0)\right)\cos^2\theta$$
$$+ \left(\frac{1}{2}L(r_0) + e_0 L(r_0)\right)\cos^2\phi\sin^2\theta \quad (3)$$

**ADVANCED
SCIENCE NEWS**

www.advancedsciencenews.com

**NANO · MICRO
small**

www.small-journal.com

Figure 1. (110) surface schematics in simple cubic structure and garnet structure. a) Schematic of the surface layer of atoms (red sphere) and missing atoms (white sphere), preserved bonds (solid black line), and broken bonds (dashed black line) on a (110) surface for a general picture of a thin film with a simple cubic structure. b) Top: a cross-section view of the (110) surface of a simple cubic structure along [001]. Bottom: a top view of the (110) surface of a simple cubic structure. Two essential symmetry breaking elements result from the broken bonds, namely, an out-of-plane inversion symmetry broken by the surface which gives rise to $K_{OOP,surface}$, and a 2-fold rotation symmetry on the (110) surface which gives rise to $K_{IP,surface}$. c) A cross-section view of the lowest energy surface in EuIG/GGG (110) determined from DFT calculations, with bulk Fe (b) and surface Fe (s) identified. d) A top view of the (110) surface. Only atoms in the boxed layers of (c) are shown. Atoms in the boxed region of (d) show a 2-fold rotation symmetry including the surface layer of atoms.

where θ and ϕ are angles in spherical polar coordinates in $(\mathbf{a}_1, \mathbf{a}_2, \mathbf{a}_3)$ space. This yields $K_{IP,\ surface} = \frac{1}{2}L(r_0) + e_0 L(r_0)$ and $K_{OOP,\ surface} = 2e_0 L(r_0)$.

3. Results

To elucidate the surface and bulk anisotropy in REIGs, we grew a thickness (t) series of EuIG (t = 5, 8, 14, 21, 26, 37, 43, 45, 53 nm) epitaxially on the (110) orientation of GGG and a thickness series of TmIG (t = 5, 12, 28 nm) on the same substrate and orientation using PLD. Yttrium iron garnet ($Y_3Fe_5O_{12}$ or YIG) of (t = 8, 12, 32 nm) was grown for comparison.

The garnet structure is cubic, $Ia\bar{3}d$, with 8 formula units within the unit cell. The atomic configuration and surface energy of the EuIG and TmIG (110) surfaces are calculated by spin-unrestricted DFT, discussed in Note S6 (Supporting Information) (Supplementary includes references).[37–41] The atomic configuration shown in Figure 1c,d gives the lowest surface energy density for both TmIG and EuIG and is therefore thermodynamically favorable. This lowest energy surface has a Fe termination with no RE atoms in the top layer. Since the Fe-O bond is lower in energy compared to the RE-O bond, this surface termination has the lowest energy. The top view of the surface atoms shown in

Figure 1d illustrates the two-fold symmetry of the lowest energy surface which allows for an IP anisotropy.

Film thickness and strain were determined through high-resolution X-ray diffraction (HR-XRD) measurements (**Figure 2a,b**). Both HR-XRD and reciprocal space mapping (RSM) measurements (Note S1, Supporting Information) showed negligible strain relaxation within the error bar, indicated by the consistent OOP strain as a function of thickness plotted in Figure 2c,d. The effect of strain variations between samples on the anisotropy extraction is discussed in Note S3 (Supporting Information). Using vibrating sample magnetometry (VSM) measurements with a field applied along the easy anisotropy axis ([110] for EuIG and [001] for TmIG), we determined the saturation magnetization (M_s) for all film thicknesses (Figure 2e,f). The bulk saturation magnetization ($M_{s,0}$) and a magnetic dead layer (t_0), which does not contribute magnetically to the film, are determined (Methods) to be 77 ± 1 kA/m and 2.9 ± 0.4 nm for EuIG and 98 ± 6 kA m^{-1} and 2.0 ± 0.1 nm for TmIG, respectively (Figure 2g,h). The bulk saturation magnetization is lower than the values reported for bulk crystals (at room temperature, 93 kA m^{-1} for EuIG and 111 kA m^{-1} for TmIG)[42] which may be a result of nonideal cation stoichiometry or oxygen content in thin films.[43] The dead layer likely originates from interdiffusion at the substrate which occurs over a distance of

ADVANCED
SCIENCE NEWS
www.advancedsciencenews.com

NANO · MICRO
small
www.small-journal.com
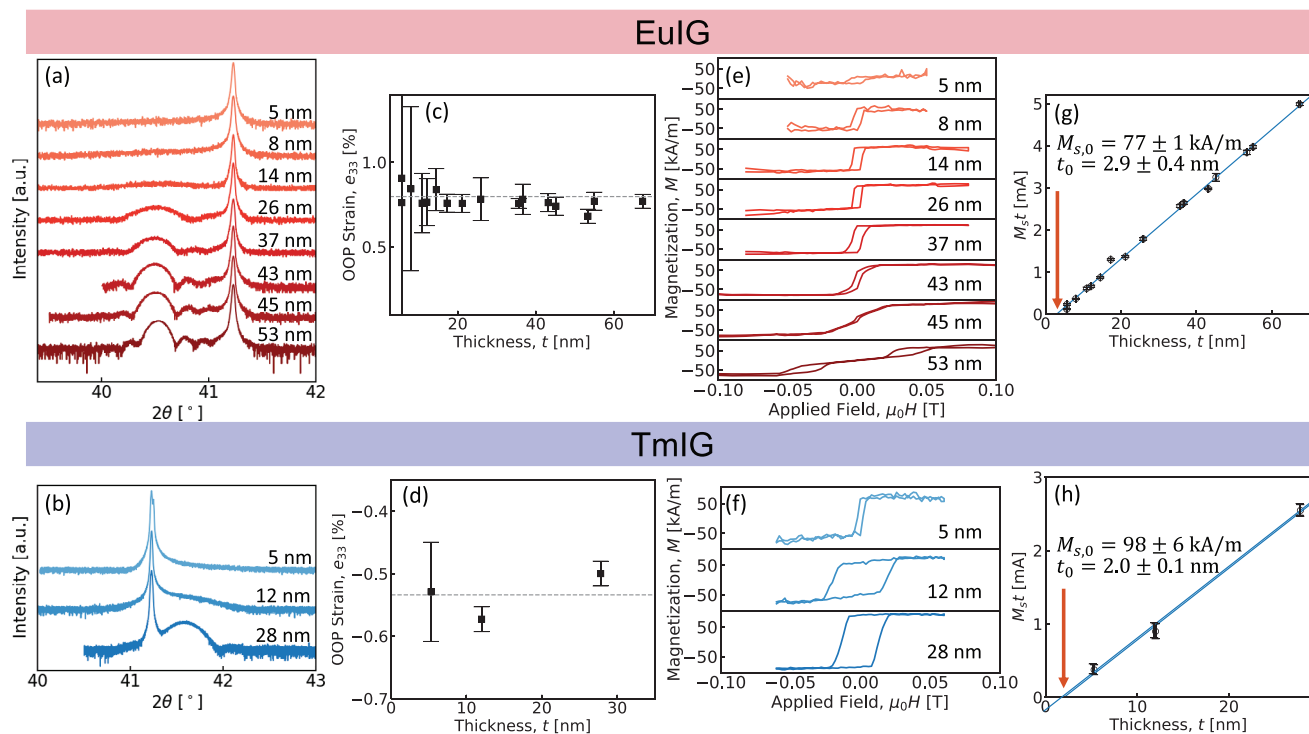
Figure 2. Sample characterization of the thickness series for EuIG/GGG (110) (top) and for TmIG/GGG (110) (bottom). a,b) HR-XRD measurements around the (440) reflection. 2θ scans reveal progressively more distinct film peaks and Laue fringes as the film thickness increases. The film peak position and Laue fringes were fitted to extract lattice spacing, film thickness, and composition. c,d) OOP strain calculated from OOP lattice spacing obtained via HRXRD. Error bars on thinner films are larger due to higher uncertainty in the fits of less pronounced film peaks. The dashed line marks the average. e,f) VSM measurements with field applied along the respective easy axes [110] ([001]) EuIG (TmIG). g,h) Bulk saturation magnetization $M_{s,0}$ and dead layer thickness t_0 are extracted from the measured saturation magnetization M_s of the individual films with thickness t through Eq. M1.

order 1 nm;[12] the room temperature Pt sputtering after break-ing vacuum leads to little interdiffusion.[44] The evolution from a square hysteresis loop in the thinner EuIG to a sheared double hysteresis loop in the thicker EuIG is a result of the transition in the lowest energy anisotropy axis from [110] to [$\bar{1}$10] together with a magnetocrystalline anisotropy which creates a four-fold symmetric energy barrier.[45] With atomic force microscopy (Figure S8, Supporting Information), we determined a surface roughness of 0.3 nm which varies little with thickness.
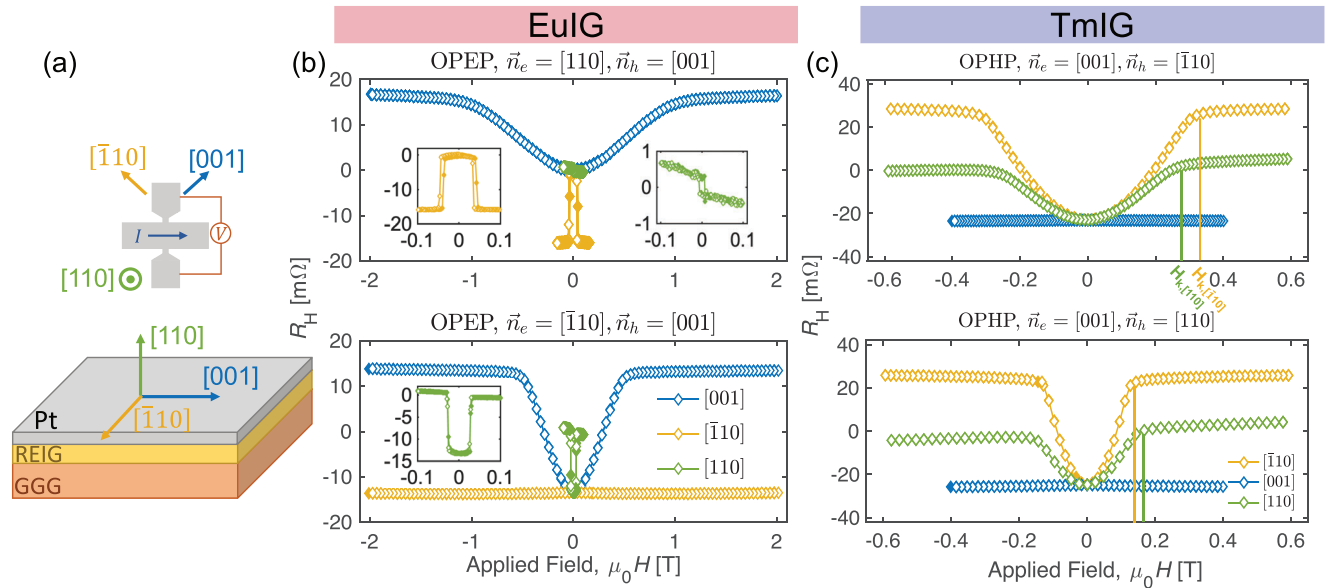
SMR measurements were performed to accurately determine the anisotropy energies along the principal axes, $a_1 = [\bar{1}10]$, $a_2 = [001]$ and $a_3 = [110]$ (Methods). With the device stack Pt (4 nm)/REIG (t nm)/GGG (110), where RE = [Eu, Tm, Y], and the device geometry shown in **Figure 3a**, we measured the trans-verse Hall voltage as a function of an applied field. A change in the equilibrium magnetization vector in the REIG by an ex-ternal field alters the spin reflectivity at the Pt/REIG interface and manifests as a variation in the transverse charge accumu-lation through the inverse spin-Hall effect.[46,47] Typical SMR curves are shown in Figure 3b for EuIG and Figure 3c for TmIG. The measured transverse Hall voltage is converted to re-sistance (R_H) by normalizing against the current $I = 0.5$ mA and plotted against the field applied along the three principal axes. SMR for the lowest energy axis shows a minimal varia-tion in R_H with the applied field, while higher energy anisotropy axes show a continuous evolution with the applied field un-

til the magnetization is saturated at the effective anisotropy field H_k.

Four different anisotropy landscapes were observed over the thickness and temperature range investigated in this study, shown schematically in Figure 3b,c. They are an OOP easy-plane (OPEP) for EuIG with the lowest energy axis along s[110] (top panel in Figure 2b) or [$\bar{1}$10] (bottom panel in Figure 3b), and an OOP hard-plane (OPHP) for TmIG with the highest energy axis along [$\bar{1}$10] (top panel in Figure 3c) or [110] (bottom panel in Figure 2c). These anisotropy landscapes arise from the interplay of magnetostatic, magnetoelastic, magnetocrystalline, growth-induced, and surface anisotropies,[42,48–50] and lead to domain patterns with IP anisotropy, specifically stripe domains in EuIG and the domain wall characters evolves with changing film thick-nesses (Figure S7, Supporting Information). The magnetoelastic contribution to the anisotropy landscape of EuIG and TmIG is a dominant factor and differs between the two material systems due to their different strain states (tensile in the plane for TmIG, compressive for EuIG) and dissimilar magnetoelastic coefficients λ. At room temperature $\lambda_{100} = 21 \times 10^{-6}$ and $\lambda_{111} = 1.8 \times 10^{-6}$ for EuIG and $\lambda_{100} = 1.4 \times 10^{-6}$ and $\lambda_{111} = -5.2 \times 10^{-6}$ for TmIG.[42]

Figure 4a,b shows the plot of extracted anisotropy energies against $1/(t - t_0)$ for EuIG and TmIG, respectively, where t is the film thickness determined by HR-XRD and t_0 is the extracted dead layer thickness (Methods B and Note S1,

**ADVANCED
SCIENCE NEWS**

www.advancedsciencenews.com

NANO · MICRO

small

www.small-journal.com

Figure 3. SMR measurement schematics and representative dataset for EuIG and TmIG. a) Schematics of the device geometry (top) for SMR measurements and the film stack (bottom). The current is aligned 45° from the IP anisotropy axes [001] and [$\bar{1}$10]. Film normal is along [110]. b) Example SMR measurements for Pt/EuIG (45 nm)/GGG (110) at − 30 °C (top) and 30 °C (bottom). The OPEP anisotropy landscape changes from having the easiest axis along [110] at − 30 °C to along [$\bar{1}$10] at 30°C. c) Pt/TmIG (5 nm)/GGG (110) at − 50 °C (top) and 50 °C (bottom). The OPHP anisotropy landscape changes from having the hardest axis along [$\bar{1}$10] at − 50 °C to [110] at 50 °C .

Supporting Information). We define the IP anisotropy energy density as $K_{IP} = E[001] − E[\bar{1}10]$ and the OOP anisotropy energy density as $K_{OOP} = E[110] − E[\bar{1}10]$. A clear $1/t$ dependence is observed in the IP anisotropy (K_{IP}) for both EuIG and TmIG over the thickness range. The OOP anisotropy (K_{OOP}) shows a $1/t$ dependence for TmIG. This trend is less clear for EuIG because the larger K_{IP} values propagate larger percentage errors to the relatively small K_{OOP}, which obscures any expected trend. Similar measurements were performed for the YIG thickness series.

We extract the surface and bulk contribution to the IP and OOP anisotropy by fitting to Equation (4) and Equation (5):

$$K_{IP} = K_{IP,bulk} + \frac{E_{IP,surface}}{t-t_0} = K_{IP,bulk} + \frac{K_{IP,surface} \cdot h}{t-t_0} \quad (4)$$

$$K_{OOP} = K_{OOP,bulk} + \frac{E_{OOP,surface}}{t-t_0} = K_{OOP,bulk} + \frac{K_{OOP,surface} \cdot h}{t-t_0} \quad (5)$$

where $K_{IP(OOP),bulk}$ is the bulk IP (OOP) anisotropy volume density and $E_{IP(OOP), surface}$ is the surface IP (OOP) anisotropy area density. The extracted anisotropy energies are summarized in **Table 1**. To provide a convenient comparison between bulk and surface anisotropy values, we convert the surface anisotropy area density to volume density using the relation, $E_{IP(OOP),surface} = K_{IP(OOP),surface} \cdot h$, where h is the thickness of surface atoms contributing to the surface anisotropy. We approximate h by the diagonal length of one unit cell (twice the (110) plane spacing), i.e., $h = a(1 + e_{33})\sqrt{2}$, where a is the lattice parameter and e_{33} is the OOP strain component. Since our choice of h is likely an overestimation of the depth of atoms affected by the free surface, $K_{IP(OOP),surface}$ represents a lower bound for its actual value.

Having established a clear signature of surface anisotropy, we explored the temperature dependence of both the surface and

bulk anisotropies by performing temperature-dependent SMR measurements for selected thicknesses of EuIG and all thicknesses of TmIG over the temperature range of 220 to 320 K. Figure 4c,d show examples of the temperature dependence of the extracted anisotropy values. Monotonic dependences on temperature were found for both a thin and thick film with slightly different gradients. (The complete data set is available in Note S4, Supporting Information). We observed a transition in the easiest (hardest) anisotropy axis in EuIG (TmIG) at T_{EPT} (T_{HPT}). In other words, the EuIG/GGG (110) maintains its hard axis of [001] through the temperature range, but within the easy (001) plane the lowest energy (easiest) direction changed from [110] to [$\bar{1}$10] as the temperature increased through T_{EPT}. For TmIG/GGG (110), the IP easy axis remained along [001] but the hardest direction in the (001) hard plane changed from [$\bar{1}$10] to [110] as the temperature increased through T_{HPT}. At the (thickness-dependent) transition temperatures, an ideal OOP easy-plane landscape is stabilized for EuIG, and an ideal OOP hard-plane is stabilized for TmIG. At these transition temperatures, the only anisotropy in the EuIG easy plane is the magnetocrystalline anisotropy, $\frac{K_{1,EuIG}}{4}$, and the only anisotropy in the TmIG hard plane is $\frac{K_{1,TmIG}}{4}$, where $K_{1,EuIG} = − 3.8 \, kJ/m^3$ and $K_{1,TmIG} = − 0.58 \, kJ \, m^{-3}$ at 300 K,[50] both of which decrease in magnitude with increasing temperature.

Since the saturation magnetization M_s also changes with temperature T, we performed temperature-dependent VSM to extract M_s over the temperature range of interest (Note S4, Supporting Information). M_s versus T was fitted with a straight line and the M_s used for the anisotropy calculation was interpolated from the fit. We extracted the temperature dependence of anisotropies by assuming a linear dependence over the measurement

**ADVANCED
SCIENCE NEWS**

www.advancedsciencenews.com

**NANO · MICRO
small**

www.small-journal.com
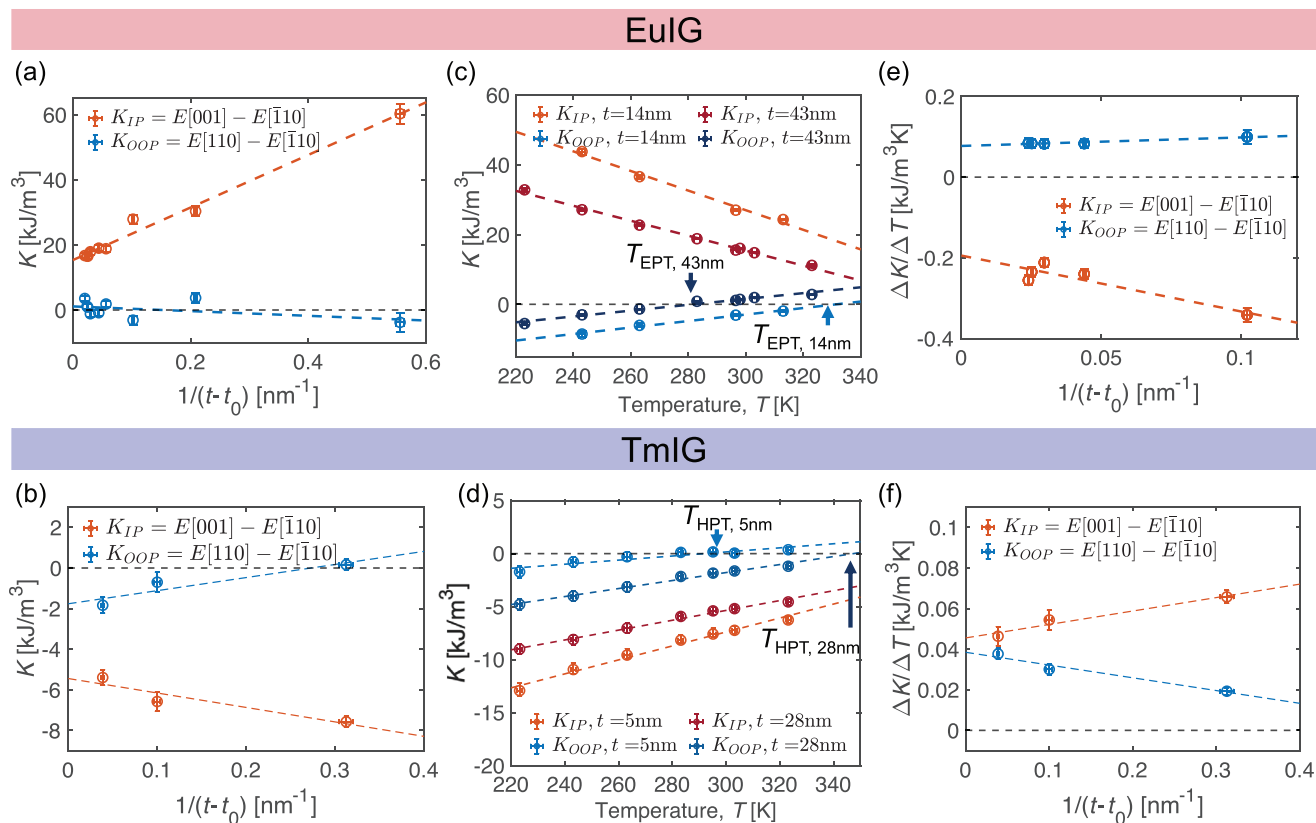
Figure 4. Anisotropy energies extracted from SMR measurements for Pt/EuIG/GGG (110) (top) and Pt/TmIG/GGG (110) (bottom). a,b) Room-temperature IP and OOP anisotropy energy K_{IP} and K_{OOP} for films of different thickness t (EuIG: $t = 5, 8, 13, 21, 26, 37, 43, 45, 53$ nm, $t_0 = 2.9$ nm; TmIG: $t = 5, 12, 28$, $t_0 = 2.0$ nm). c,d) Examples of the monotonic temperature dependence of the extracted anisotropy values for a thin and thick film. A transition in the easiest (hardest) anisotropy axis is observed in EuIG (TmIG) at T_{EPT} (T_{HPT}). At the transition temperature, an ideal OPEP (OPHP) is stabilized with only magnetocrystalline anisotropy $K_1/4$ in the plane. e,f) Temperature dependence of the anisotropies ($\Delta K/\Delta T$) as a function of film thickness to extract the temperature dependence of the bulk and surface anisotropies.

temperature range. From the plot of $\Delta K/\Delta T$ against $1/(t - t_0)$ in Figure 4e,f, we obtained the temperature dependence of the bulk and surface anisotropies for Pt/EuIG/GGG and Pt/TmIG/GGG, respectively.

Figure 5a shows a side-by-side comparison of the extracted anisotropy energies of EuIG, TmIG, and YIG (complete data for YIG is included in Note S6, Supporting Information). The results indicate the presence of surface anisotropy which has both IP and OOP contributions. The surface anisotropy includes contributions from both the film-substrate interface and the film-Pt interface. Both interfaces are 2-fold symmetric and the structural symmetry breaking contributes to both IP and OOP surface anisotropy terms through the Néel surface model.

Both EuIG and TmIG show a large IP surface anisotropy, in contrast to a negligible IP surface anisotropy in YIG, while YIG shows a larger OOP surface anisotropy compared to EuIG and TmIG. The IP surface anisotropy is more substantial in EuIG than in TmIG which could be related to a larger magnetoelastic coefficient and lattice mismatch strain in EuIG. Negligible surface and bulk IP anisotropies are measured in YIG since both SOC and lattice mismatch strain are negligible ($a_{YIG} = a_{GGG} = 12.376$ Å). Although a weak IP anisotropy could be present, it is in the J/m³ range which is orders of magnitude

smaller compared to other terms[51] and hence not discussed here.

We can consider YIG as a control dataset to disentangle the effect of Rashba SOC resulting from the Pt layer. Rashba SOC has a different symmetry compared to the Néel surface anisotropy, specifically, it induces an OOP surface anisotropy with no component in the film plane.[52,53] In the thickness series of YIG, we observed a large OOP surface anisotropy and negligible IP surface anisotropy, which agrees with the symmetry of Rashba SOC-induced surface anisotropy. Our Pt/YIG/GGG (110) films yielded an OOP surface anisotropy of 0.035 mJ m⁻² which matches well with the previously reported value for Rashba SOC-induced interfacial anisotropy in Pt/BiYIG/GSGG (111) films.[53] According to Equation (3), the OOP Néel surface anisotropy exists for a simple cubic structure only when the lattice mismatch strain is nonzero. We hypothesize that the Néel surface anisotropy in YIG is negligible because of the negligible lattice mismatch, and Rashba SOC from Pt dominantly contributes to the surface anisotropy in YIG. Conversely, both Néel surface anisotropy and Rashba SOC contribute to EuIG and TmIG. Given Y³⁺ is not a magnetic ion and has negligible SOC, the Néel surface anisotropy could be strongly correlated to the SOC strength of the rare-earth element in the garnet thin film. The Rashba SOC effects in EuIG and TmIG are

Table 1. Extracted bulk and surface anisotropies for EuIG, TmIG, and YIG, with the bulk contribution to IP (OOP) anisotropy energy density, $K_{IP(OOP),bulk}$ and the surface contribution to IP (OOP) anisotropy energy density, $K_{IP(OOP),surface}$. The volume density, $K_{IP(OOP),surface}$ was converted from an area density, $E_{IP(OOP),surface}$ with the approximation of $h = a(1 + e_{33})\sqrt{2}$, where h is the thickness of the layer contributing to surface anisotropy and a is the lattice parameter, $h_{EuIG} = 1.78$ nm, $h_{TmIG} = 1.74$ nm and $h_{YIG} = 1.75$ nm. The magnetostatic contribution, $K_{MS} = \frac{1}{2} \mu_0 M_s^2$, is subtracted from $K_{OOP,bulk}$.

	$K_{IP,bulk}$ [kJ/m³]	$K_{OOP,bulk} - K_{MS}$ [kJ/m³]	$E_{IP,surface}$ [µJ/m²]	$K_{IP,surface}$ [kJ/m³]	$E_{OOP,surface}$ [µJ/m²]	$K_{OOP,surface}$ [kJ/m³]
EuIG	15.3 ± 0.8	− 2.6 ± 1.0	81 ± 4	45 ± 2	− 7 ± 5	− 4 ± 3
TmIG	− 5.4 ± 0.6	− 7.8 ± 0.5	− 6 ± 3	− 3.7 ± 1.7	6 ± 2	3.4 ± 1.4
YIG	0.0 ± 0.5	1.2 ± 0.4	0 ± 1	0.0 ± 0.5	35 ± 2	20 ± 1
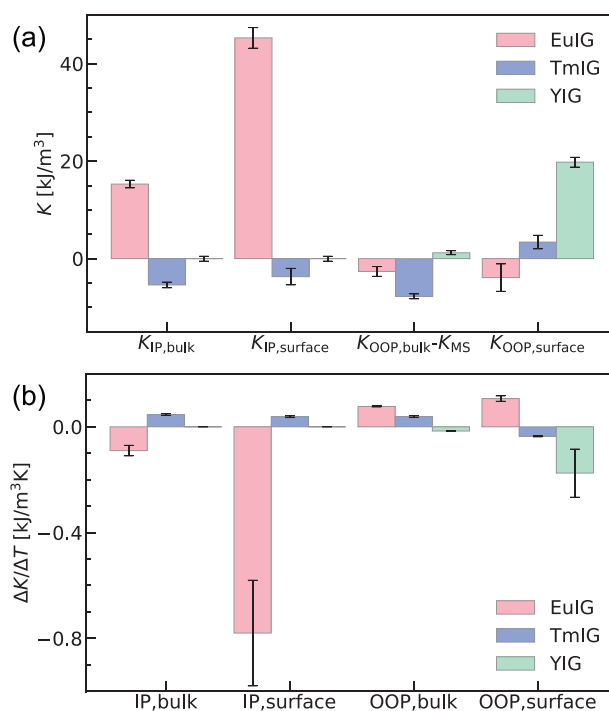
Figure 5. Summary plot of extracted anisotropies and their temperature dependence. a) Comparison of the extracted bulk and surface anisotropies for EuIG, TmIG, and YIG, with $K_{IP(OOP),bulk}$ the bulk contribution to IP (OOP) anisotropy energy density, $K_{IP(OOP),surface}$ the surface contribution to IP (OOP) anisotropy energy density converted from an areal density to volume density with the assumption of $h = a(1 + e_{33})\sqrt{2}$, where h is the thickness of the layer contributing to surface anisotropy and a is the lattice parameter. $h_{EuIG} = 1.78$ nm, $h_{TmIG} = 1.74$ nm, and $h_{YIG} = 1.75$ nm. $K_{OOP,bulk} - K_{MS}$ is plotted to remove the effect of demagnetization field in a thin film which contributes to the magnetostatic anisotropy K_{MS}. b) Comparison of the extracted temperature dependence $\Delta K / \Delta T$ of the bulk and surface anisotropies for EuIG, TmIG, and YIG.

expected to be on the same order of magnitude as in YIG due to their similar origin from the Pt overlayer. Therefore, we propose that Néel surface anisotropy contributes with a sign opposite to the Rashba SOC in both EuIG and TmIG and cancels most of the Rashba SOC surface anisotropy.

Surface anisotropy decreases with increasing temperature (Figure 5b), consistent with the Néel surface anisotropy model. This is reflected by a change in sign between the anisotropy energies at room temperature and their temperature dependence ($\Delta K / \Delta T$). Both the bulk and surface anisotropy have a negative temperature coefficient, consistent with the consideration of Néel surface anisotropy where the interaction energies between pairs of atoms and the magnetization decrease in strength with weaker SOC at elevated temperatures.[12] Previous work on the temperature dependence of surface anisotropy in metallic systems showed the same trend.[54]

Finally, we discuss other possible origins of the observed surface anisotropy. If surface anisotropy is dominated by strain relaxation in the surface layer of atoms, the surface anisotropy will contribute to lowering the total anisotropy energy for thinner films compared to thicker ones. However, an increase in anisotropy energy is observed in thinner films which contradicts

RIGHTSLINK

this hypothesis. RSM and rocking curve measurements also did not support a thickness dependence of the strain state. Furthermore, atom probe tomography of a TmIG film showed that the Tm:Fe composition ratio did not vary with depth (Note S1, Supporting Information). If the assumption for a constant M_s for all thicknesses is invalid, i.e., instead of a magnetic dead layer, the M_s is smaller in thinner films due to, e.g., point defects or interdiffusion, the total anisotropy energies calculated using the M_s from VSM would be approximately the same for all film thicknesses. However, this requires the single-ion anisotropy constant to be higher for thinner films which is implausible.

We therefore propose that there is a significant Néel surface anisotropy in our Pt/REIG/GGG. Despite the large number of atoms within a REIG unit cell and the complex crystal structure, there exists a lowest energy surface that dominates the nucleation and growth during film deposition, consistent with the sub-unit cell layer-by-layer growth of YIG observed by reflection high energy electron diffraction.[55,56] From the crystal structure, there are four types of distinguishable surface terminations in a REIG with (110) orientation, and our DFT calculations revealed that the surface configuration shown in Figure 1c,d has the lowest energy. This surface preserves RE-O bonds, and only the lower energy Fe-O bonds are broken (Note S6, Supporting Information). With the lowest energy surface being the dominant termination after film deposition, we can account for the consistency of the surface anisotropy measured across samples.

4. Discussion

We demonstrated that the inversion symmetry breaking at the (110) surface of an epitaxial complex oxide thin film can result in a surface contribution to the IP anisotropy, which can be explained by the phenomenological Néel surface model. Significant IP surface anisotropy is observed in heterostructures of two different REIGs, Pt/EuIG/GGG and Pt/TmIG/GGG, in contrast to negligible IP surface anisotropy in Pt/YIG/GGG, where the SOC strength and strain are negligible compared to those of EuIG and TmIG. However, the OOP surface anisotropy is complicated by the Rashba–induced isotropic IP anisotropy introduced by the heavy metal (Pt) overlayer which was required for SMR measurement. With the dataset for YIG as the control, we infer that the contribution from the Néel surface anisotropy is opposite to the Rashba contribution from Pt. Future work could characterize the surface anisotropy with bare films using angle-dependent ferromagnetic resonance measurements to deconvolve the contributions.

The variety of anisotropy landscapes tunable through thickness and temperature provide platforms for the exploration of dynamics and devices unprecedented in a simple uniaxial anisotropy system. Novel phenomena of exchange-driven auto-oscillation in the terahertz regime and coherent magnon transport through spin superfluidity have been proposed in systems with an OPEP anisotropy landscape.[22–25,57] More efficient IP switching has been predicted in systems with an OPHP anisotropy landscape.[26] The substantial IP surface anisotropy gives rise to a stronger easy plane anisotropy for Pt/EuIG/GGG and hard plane anisotropy for Pt/TmIG/GGG as the film becomes thinner, which makes them suitable candidates for these applications.

5. Experimental Section

Sample Preparation and Characterization: The EuIG, TmIG, and YIG thin films were grown on GGG (110) substrates (MTI Corporation) by PLD with a 248 nm wavelength KrF excimer laser at an energy of 350 mJ and a repetition rate of 5 Hz using a thickness-to-shot calibration of 50 nm per 10k shots. The targets were commercially available EuIG, TmIG, and YIG sintered disks with a 99.99% elemental purity. The growth atmosphere was oxygen at 150 mTorr with a base pressure of 5×10^{-6} Torr and the substrate temperature was 750 °C. HR-XRD measurements of the (440) reflection were performed on a Bruker D8 HR-XRD and the data was fitted to determine the film thickness and the strain from the (110) plane spacing. RMS measurements were performed on a Rigaku Smartlab X-ray diffractometer to map the IP and OOP lattice spacing. The saturation magnetization was determined using VSM. Assuming a dead (low magnetization) layer (t_0), caused for example by the interdiffusion of Ga and Fe atoms between the substrate and the film, the bulk saturation magnetization $M_{s,0}$ and magnetic dead layer t_0 were determined by plotting $M_s t$ against t, i.e., fitting to Equation M1. This agrees with a previously reported dead layer of 1.4 nm in TmIG grown on a GGG (111) substrate under similar conditions.[12]

$$M_s t = M_{s,0} \ (t - t_0) \tag{6}$$

SMR Measurements: 4 nm Pt was sputtered on EuIG (t nm)/GGG (110), TmIG (t nm)/GGG (110), and YIG (t nm)/GGG (110) from a 1 inch Pt target using a d.c. sputter system with an Ar pressure of 3 mTorr and base pressure of 5×10^{-8} Torr. Hall crosses with a typical active area dimension of 100 × 100 μm were patterned using standard photolithography and ion milling. The current arm of the device was aligned to 45 degrees from the IP principal anisotropy axes to maximize the signal.[45–47] Ta (6)/Au (150) contacts were patterned through lift-off.

SMR measurements were performed on a custom-built transport measurement setup at room temperature for Figure 3a,b. Temperature-dependence measurements were performed on the same setup including with cryogenic control and the temperature being read from a thermocouple mounted on the sample holder. The current was applied through an SR830 lock-in amplifier at a frequency of 9.973 kHz and a voltage amplitude of 5 V. A 10 kΩ resistor was connected in series with the device (with a typical resistance <100 Ω) to provide a stable current source of 0.5 mA. The transverse voltage was measured through the lock-in amplifier. The transverse magnetoresistance can be expressed in Equation M2, where $\phi_I = 45°$.

$$R_H = R_{SMR,AHE} \ \cos\theta + R_{SMR}\sin^2\theta \sin 2 \ (\phi - \phi_I) + R_{OHE}\mu_0 H_3 \tag{7}$$

The anisotropy energies were obtained by fitting the SMR data with a macrospin model to minimize the total energy in the presence of an applied field and an anisotropy field. The detailed fitting protocols are discussed in Note S2 (Supporting Information). Discussion on the magnetization reversal behavior in EuIG with an OPEP anisotropy landscape can be found in our previous work.[45]

Statistical Analysis: Statistical analysis of data was carried out using Matlab software and Python packages through least-squares fit. Anisotropy energy values were obtained by fitting to SMR curves, which typically contain 100 data points in each scan. For extraction of bulk and surface anisotropy energies, all data points used for fitting were plotted, and the error bars were obtained from the covariance of the linear fit. Further error analysis associated with specific measurements can be found in the Supporting Information.

Supporting Information

Supporting Information is available from the Wiley Online Library or from the author.

Conflict of Interest

The authors declare no conflict of interest.

Author contributions

Y.S. and K.L. contributed equally to this work. Y.S., G.S.D.B., and C.A.R. conceived the project. Y.S. and K.L. planned and conducted the experiments. Y.S. prepared the samples. H.T. performed DFT calculations. Y.S., K.L., H.T., G.S.D.B., and C.A.R. analyzed the data and wrote the manuscript. all authors contributed to the discussion of the data in the manuscript.

Data Availability Statement

The data that support the findings of this study are available in the supplementary material of this article.

[1] S. Ikeda, K. Miura, H. Yamamoto, K. Mizunuma, H. D. Gan, M. Endo, S. Kanai, J. Hayakawa, F. Matsukura, H. Ohno, *Nat. Mater.* **2010**, *9*, 721.

[2] B. Dieny, M. Chshiev, *Rev. Mod. Phys.* **2017**, *89*, 025008.

[3] S. Parkin, S.-H. Yang, *Nat. Nanotechnol.* **2015**, *10*, 195.

[4] S. I. Kiselev, J. C. Sankey, I. N. Krivorotov, N. C. Emley, R. J. Schoelkopf, R. A. Buhrman, D. C. Ralph, *Nature* **2003**, *425*, 380.

[5] M. Krawczyk, D. Grundler, *J. Phys.: Condens. Matter* **2014**, *26*, 123202.

[6] M. Bibes, A. Barthelemy, *IEEE Trans. Electron Devices* **2007**, *54*, 1003.

[7] F. Trier, P. Noël, J.-V. Kim, J.-P. Attané, L. Vila, M. Bibes, *Nat. Rev. Mater.* **2021**, *7*, 258.

[8] R. Cheng, M. W. Daniels, J.-G. Zhu, D.i Xiao, *Phys. Rev. B* **2015**, *91*, 064423.

[9] A. Stupakiewicz, C. S. Davies, K. Szerenos, D. Afanasiev, K. S. Rabinovich, A. V. Boris, A. Caviglia, A. V. Kimel, A. Kirilyuk, *Nat. Phys.* **2021**, *17*, 489.

[10] L. J. Cornelissen, J. Liu, R. A. Duine, J. B. Youssef, B. J. van Wees, *Nat. Phys.* **2015**, *11*, 1022.

[11] R. Timalsina, H. Wang, B. Giri, A. Erickson, X. Xu, A. Laraoui, *Adv. Electron. Mater.* **2024**, *10*, 2300648.

[12] L. Caretta, E. Rosenberg, F. Büttner, T. Fakhrul, P. Gargiani, M. Valvidares, Z. Chen, P. Reddy, D. A. Muller, C. A. Ross, G. S. D. Beach, *Nat. Commun.* **2020**, *11*, 1090.

[13] S. Vélez, S. Ruiz-Gómez, J. Schaab, E. Gradauskaite, M. S. Wörnle, P. Welter, B. J. Jacot, C. L. Degen, M. Trassin, M. Fiebig, P. Gambardella, *Nat. Nanotechnol.* **2022**, *17*, 834.

[14] S. Ding, A. Ross, D. Go, L. Baldrati, Z. Ren, F. Freimuth, S. Becker, F. Kammerbauer, J. Yang, G. Jakob, Y. Mokrousov, M. Kläui, *Phys. Rev. Lett.* **2020**, *125*, 177201.

[15] A. Quindeau, C. O. Avci, W. Liu, C. Sun, M. Mann, A. S. Tang, M. C. Onbasli, D. Bono, P. M. Voyles, Y. Xu, J. Robinson, G. S. D. Beach, C. A. Ross, *Adv. Electron. Mater.* **2017**, *3*, 1600376.

[16] E. R. Rosenberg, L. S. Beran, C. O. Avci, C. Zeledon, B. Song, C. Gonzalez-Fuentes, J. Mendil, P. Gambardella, M. Veis, C. Garcia, G. S. D. Beach, C. A. Ross, *Phys. Rev. Mater.* **2018**, *2*, 094405.

[17] L. Soumah, N. Beaulieu, L. Qassym, C. Carrétéro, E. Jacquet, R. Lebourgeois, J. Ben Youssef, P. Bortolotti, V. Cros, A. Anane, *Nat. Commun.* **2018**, *9*, 3355.

[18] C. O. Avci, A. Quindeau, C.-F. Pai, M. Mann, L. Caretta, A. S. Tang, M. C. Onbasli, C. A. Ross, G. S. D. Beach, *Nat. Mater.* **2017**, *16*, 309.

[19] L. Caretta, S.e-H. Oh, T. Fakhrul, D.-K. Lee, B. H. Lee, S.e K. Kim, C. A. Ross, K.-J. Lee, G. S. D. Beach, *Science* **2020**, *370*, 1438.

[20] J. F. Nye, *Physical Properties Of Crystals: Their Representation By Tensors And Matrices*, Oxford University Press, Oxford, United Kingdom, **1984**.

[21] M. Hoffmann, B. Zimmermann, G. P. Müller, D. Schürhoff, N. S. Kiselev, C. Melcher, S. Blügel, *Nat. Commun.* **2017**, *8*, 308.

[22] O. R. Sulymenko, O. V. Prokopenko, V. S. Tiberkevich, A. N. Slavin, B. A. Ivanov, R. S. Khymyn, *Phys. Rev. Appl.* **2017**, *8*, 064007.

[23] R. Cheng, D. Xiao, A. Brataas, *Phys. Rev. Lett.* **2016**, *116*, 207603.

[24] D. Marković, M. W. Daniels, P. Sethi, A. D. Kent, M. D. Stiles, J. Grollier, *Phys. Rev. B* **2022**, *105*, 014411.

[25] E. A. Montoya, A. Khan, C. Safranski, A. Smith, I. N. Krivorotov, *Commun. Phys.* **2023**, *6*, 184.

[26] Y. Zhou, C. Guo, C. Wan, X. Chen, X. Zhou, R. Zhang, Y. Gu, R. Chen, H. Wu, X. Han, F. Pan, C. Song, *Phys. Rev. Appl.* **2020**, *13*, 064051.

[27] H. Lüth, *Surfaces and Interfaces of Solid Materials*, Springer, Berlin Heidelberg, **1995**.

[28] W. Mönch, *Semiconductor Surfaces and Interfaces*, Springer, Berlin Heidelberg, **2001**.

[29] L. Néel, *Comptes Rendus Hebdomadaires Des Seances De L Academie Des Sciences* **1953**, *237*, 1468.

[30] M. T. Johnson, R. Jungblut, P. J. Kelly, F. J. A. den Broeder, *J. Magn. Magn. Mater.* **1995**, *148*, 118.

[31] S. Monso, B. Rodmacq, S. Auffret, G. Casali, F. Fettar, B. Gilles, B. Dieny, P. Boyer, *Appl. Phys. Lett.* **2002**, *80*, 4157.

[32] D. S. Chuang, C. A. Ballentine, R. C. O'Handley, *Phys. Rev. B* **1994**, *49*, 15084.

[33] R. H. Victora, J. M. MacLaren, *Phys. Rev. B* **1993**, *47*, 11583.

[34] U. Gradmann, J. Korecki, G. Waller, *Applied Physics A Solids and Surfaces* **1986**, *39*, 101.

[35] C. Chappert, P. Bruno, *J. Appl. Phys.* **1988**, *64*, 5736.

[36] G. F. Dionne, *Magnetic Oxides*, Springer, Berlin, Germany, **2009**.

[37] R. Zeller, *Computational Nanoscience* **2006**, *31*, 74419.

[38] G. Kresse, D. Joubert, *Phys. Rev. B* **1999**, *59*, 1758.

[39] G. Kresse, J. Furthmüller, *Phys. Rev. B* **1996**, *54*, 11169.

[40] J. P. Perdew, K. Burke, M. Ernzerhof, *Phys. Rev. Lett.* **1996**, *77*, 3865.

[41] H. J. Monkhorst, J. D. Pack, *Phys. Rev. B* **1976**, *13*, 5188.

[42] A. H. Eschenfelder, *Magnetic Bubble Technology*, Springer, Berlin Heidelberg, **1980**.

[43] E. Rosenberg, J. Bauer, E. Cho, A. Kumar, J. Pelliciari, C. A. Occhialini, S. Ning, A. Kaczmarek, R. Rosenberg, J. W. Freeland, Y. Chen, J. Wang, J. LeBeau, R. Comin, F. M. F. De Groot, C. A. Ross, *Small* **2023**, *19*, 2300824.

ADVANCED
SCIENCE NEWS

www.advancedsciencenews.com

NANO · MICRO
small
www.small-journal.com

[44] J. J. Bauer, P. Quarterman, A. J. Grutter, B. Khurana, S. Kundu, K. A. Mkhoyan, J. A. Borchers, C. A. Ross, *Phys. Rev. B* **2021**, *104*, 094403.

[45] Y. Song, A. C. Kaczmarek, G. S. D. Beach, C. A. Ross, *Phys. Rev. Mater.* **2023**, *7*, 084407.

[46] Y.-T. Chen, S. Takahashi, H. Nakayama, M. Althammer, S. T. B. Goennenwein, E. Saitoh, G. E. W. Bauer, *Phys. Rev. B* **2013**, *87*, 144411.

[47] H. Nakayama, M. Althammer, Y.-T. Chen, K. Uchida, Y. Kajiwara, D. Kikuchi, T. Ohtani, S. Geprägs, M. Opel, S. Takahashi, R. Gross, G. E. W. Bauer, S. T. B. Goennenwein, E. Saitoh, *Phys. Rev. Lett.* **2013**, *110*, 206601.

[48] H. Callen, *Appl. Phys. Lett.* **1971**, *18*, 311.

[49] A. C. Kaczmarek, E. R. Rosenberg, Y. Song, K. Ye, G. A. Winter, A. N. Penn, R. Gomez-Bombarelli, G. S. D. Beach, C. A. Ross, *Nat. Commun.* **2024**, *15*, 5083.

[50] S. M. Zanjani, M. C. Onbaşlı, *Data in Brief* **2020**, *28*, 104937.

[51] J. Mendil, M. Trassin, Q. Bu, J. Schaab, M. Baumgartner, C. Murer, P. T. Dao, J. Vijayakumar, D. Bracher, C. Bouillet, C. A. F. Vaz, M. Fiebig, P. Gambardella, *Phys. Rev. Mater.* **2019**, *3*, 034403.

[52] A. J. Lee, A. S. Ahmed, B. A. McCullian, S. Guo, M. Zhu, S. Yu, P. M. Woodward, J. Hwang, P. C. Hammel, F. Yang, *Phys. Rev. Lett.* **2020**, *124*, 257202.

[53] B. H. Lee, T. Fakhrul, C. A. Ross, G. S. D. Beach, *Phys. Rev. Lett.* **2023**, *130*, 126703.

[54] M. Farle, W. Platow, A. N. Anisimov, B. Schulz, K. Baberschke, *J. Magn. Magn. Mater.* **1997**, *165*, 74.

[55] C. Tang, M. Aldosary, Z. Jiang, H. Chang, B. Madon, K. Chan, M. Wu, J. E. Garay, J. Shi, *Appl. Phys. Lett.* **2016**, *108*, 102403.

[56] Y. Krockenberger, K.-S. Yun, T. Hatano, S. Arisawa, M. Kawasaki, Y. Tokura, *J. Appl. Phys.* **2009**, *106*, 123911.

[57] S. o Takei, Y. Tserkovnyak, *Phys. Rev. Lett.* **2014**, *112*, 227201.

2407381 (10 of 10)

Temperature-dependent Surface Anisotropy in (110) Epitaxial Rare Earth Iron Garnet Films

Supplementary Information

Yixuan Song[1]*, Katharina Lasinger[1,2]*, Hao Tang[1], Ju Li[1,3], Geoffrey S. D. Beach[1] and Caroline C. A. Ross[1]

[1] *Department of Materials Science and Engineering, Massachusetts Institute of Technology, Cambridge, Massachusetts, 02139, USA*
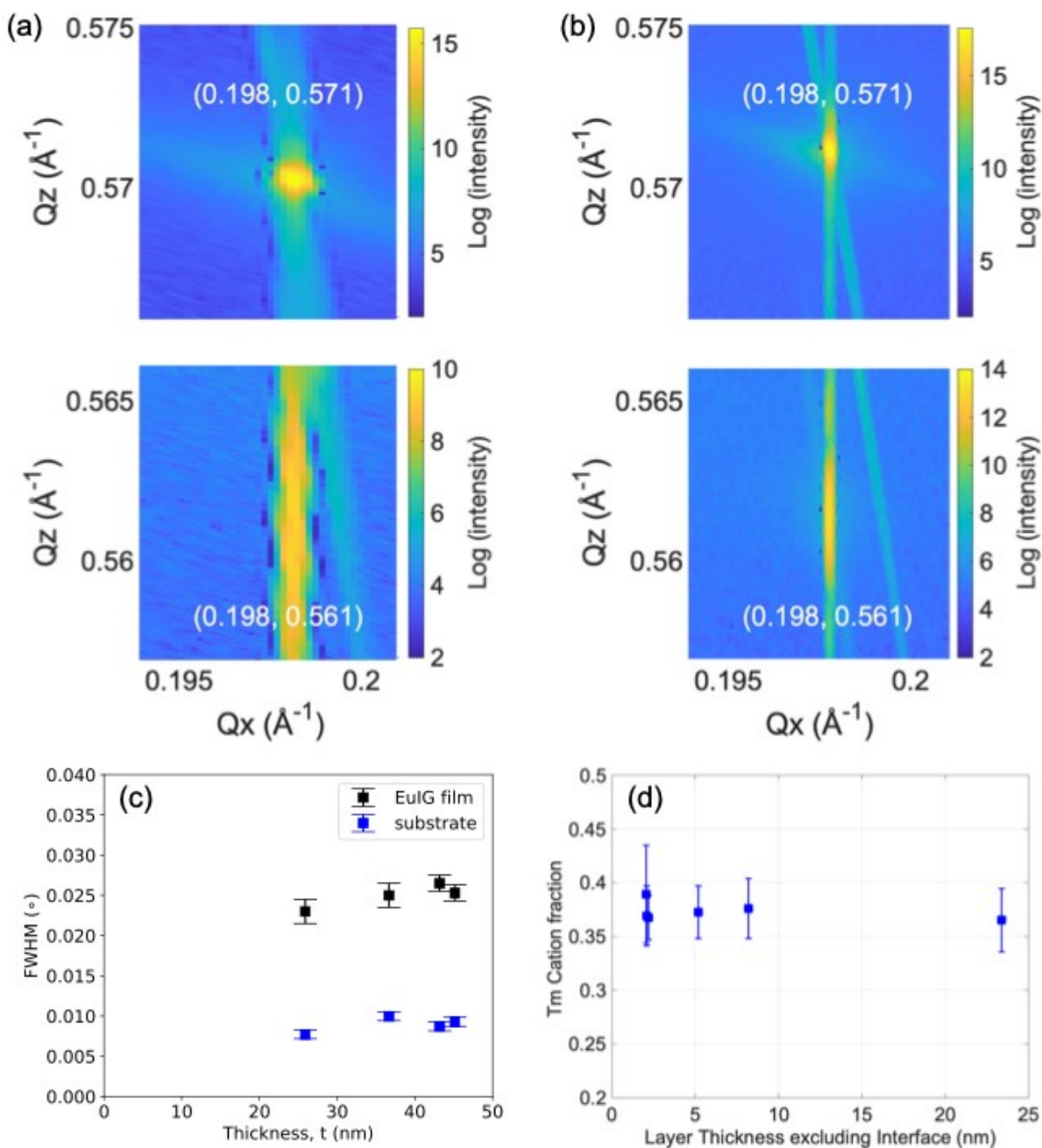
[2] *Department of Materials Science, ETH Zurich, 8093 Zurich, Switzerland*

[3] *Department of Nuclear Science and Engineering, Massachusetts Institute of Technology, Cambridge, Massachusetts, 02139, USA*

Supplemental Information

Contents   ***Page***

*Authors contributed equally to this work

Fig. S1. Reciprocal space map (RSM) for the (642) reflection of EuIG/GGG (110) films with thicknesses of **(a)** 14nm and **(b)** 45nm. The top panels show the reflections corresponding to the substrate and the bottom panels show the reflections corresponding to the film. The coordinates

labeled in white correspond to the fitted peak positions. The substrate and film peaks are plotted in different panels because of the difference in intensity. (c) FWHM of the omega-scan (rocking curve) measurement for the (440) reflection in the EuIG films and the GGG substrates. (d) Tm cation ratio as a function of TmIG thickness extracted from the APT measurement of a 1D-concentration profile along the long axis of the tip.

(i) X-ray diffraction

High-resolution X-ray diffraction (HRXRD) measurements were performed on the (440) reflection for all films to determine their thicknesses. Film thicknesses were obtained from fitting to the Laue fringes of HRXRD and additional x-ray reflectivity (XRR) measurements were performed for thinner samples where the Laue fringes are less clear from HRXRD, and thicknesses were determined from fitting to the Kiessig fringes.

Using a combination of reciprocal space map (RSM) and HRXRD measurements, we determined the strain tensor (Eq. S1) with the coordination system defined by $\boldsymbol{a_1} = [\bar{1}10]$, $\boldsymbol{a_2} = [001]$ and $\boldsymbol{a_3} = [110]$. From RSM for EuIG with film thicknesses of 14 nm, 48 nm and 67 nm in Fig S1, we observe that the dominant film peak has the same Q_x value as the substrate peak, indicating an in-plane lattice matching as the film thickness increases from 14 nm to 45 nm. No additional peaks that correspond to strain relaxed film which causes Q_x to be different between film peak and substrate peak were observed. Therefore, we can assume uniform in-plane strain of $e_{11} = e_{22} = e_0 = \frac{a_{GGG}-a_{REIG}}{a_{REIG}}$. We attribute this strain coherency in thicker films to a high thermodynamic and kinetic energy barrier for dislocation nucleation in complex oxides.

We determined the out-of-plane spacing for (440) planes (d_{440}) from the 2θ values obtained by fitting to the film peak (around 40.5° for EuIG and around 41.6° for TmIG). We calculated the out-of-plane strain as $e_{33} = \frac{d_{440}/4\sqrt{(2)}-a_{REIG}}{a_{REIG}}$ which is plotted in Fig. 2(c) and (d). $e_{ij} = 0, \forall i \neq j$ since the coordinate system corresponds to principal strain axes. The Poisson ratio was calculated from $e_{33}/e_0 = -\frac{2v}{1-v}$, using the average value of e_{33} from all thicknesses. We obtained $v = 0.29$ for EuIG and $v = 0.38$ for TmIG.

$$e = \begin{pmatrix} e_{11} & e_{12} & e_{13} \\ e_{21} & e_{22} & e_{23} \\ e_{31} & e_{32} & e_{33} \end{pmatrix} = e_0 \begin{pmatrix} 1 & 0 & 0 \\ 0 & 1 & 0 \\ 0 & 0 & e_{33}/e_0 \end{pmatrix} \qquad (S1)$$

The error in e_{33} is estimated by considering the contributions from fitting and instrument resolution. The fitting uncertainty in from d_{110} is obtained from fitting to HRXRD using Rigaku GlobalFit software. Instrument resolution is $\delta\theta = 0.0005^\circ = 9 \times 10^{-6} rad$. From the Bragg diffraction criterion $2d_{440}\sin\theta_{440} = \lambda$, we obtain $\frac{\delta d_{440}}{d_{440}} = \frac{\delta d_{110}}{d_{110}} = \frac{1}{\tan\theta_{440}}\delta\theta$. This leads to $\delta d_{110} = 2\times 10^{-5}d_{110}$. Two uncorrelated errors propagate as $\delta d_{110} = \sqrt{\left(\delta d_{110,fit}\right)^2 + \left(\delta d_{110,instr}\right)^2}$. From the definition of $e_{33} = \frac{d_{110}-a_{REIG}}{a_{REIG}}$, we obtain an error in e_{33} contributed by fitting of $\delta e_{33} = \frac{\delta d_{110}}{a_{REIG}}$.

In addition, we performed omega scan (rocking curve) measurements on the (440) film and substrate peak and calculated the FWHM of the film as a function of the film thickness as shown in Fig. S1(c). A small and constant FWHM is observed for all thicker films, suggesting that the strain state has a similar amount of inhomogeneity across the range of film thicknesses, i.e. there is not a strain relaxation throughout the thickness.

(ii) Atom probe tomography

We measured the cation stoichiometry using atom probe tomography (APT) of a range of TmIG film thicknesses (2-8 nm) shown in Fig. S1(d). No variation in Tm^{3+} cation ratio outside the measurement error bar is observed. The extracted cation fractions for both rare-earth elements and iron are in good agreement with the expected values, i.e. 3/8 = 0.375 for the rare-earth elements and 5/8 = 0.625 for iron. The X-ray and APT data indicate that changes in stoichiometry and strain state with thickness are not significant and would therefore not explain the thickness-dependent anisotropy.

(ii) Vibrating sample magnetometry

Angle dependent vibrating sample magnetometry (VSM) was performed to determine the saturation magnetization and identify the in-plane easy and in-plane hard anisotropy axes (Fig. 2 (e) and (f)). To this extent, we took measurements with an in-plane magnetic field applied at

angles of $\pm 35°$ and $\pm 55°$ relative to the cut substrate edge (MTI Corporation substrates with $\langle 11\bar{1}\rangle$ edges). These directions correspond to $[\bar{1}10]$ and $[001]$, respectively, which are the in-plane principal anisotropy axes for EuIG and TmIG films on GGG substates on the (110) orientation. The square hysteresis loops shown in Fig. 2 (e) and (f) with field applied along $[110]$ for EuIG and $[001]$ for TmIG reveal in-plane easy axes along $[110]$ and $[001]$, respectively. Additional hysteresis features observed in the thicker films are explained in our previous work as a result of the magnetocrystalline anisotropy which creates a barrier between the local minimum $[110]$ and $[\bar{1}10]$ states [40]. The saturation fields along the hard anisotropy axis ($[001]$ for EuIG and $[\bar{1}10]$ for TmIG) were too high to be quantified via VSM since the paramagnetic GGG introduces a large non-linear background at high fields. We note that YIG films on GGG(110) substrates exhibit in-plane isotropic magnetization vs. field behavior indicative of an in-plane easy plane configuration (SI Note 6).

We extracted the saturation magnetization $M_{s,0}$ from the easy-axes measurements for each film within a thickness series of the same composition. Subsequently, to determine the bulk saturation magnetization and the thickness of the magnetically inactive layer t_0, the product $M_s t$ is fitted to Eq. S2. The fitted result is shown in Fig. 2 (g) and (h).

$$M_s t = M_{s,0}(t - t_0) \qquad (S2)$$

Typically, the VSM measurements were taken with a field range of -0.15 T to 0.15 T. For the analysis, we select data points up to a certain cut-off field to exclude the non-linear contribution from the substrate. We then select a number of data points in both saturation regimes at positive and negative fields and perform a linear background subtraction. The saturation magnetization is estimated through a linear fit to the saturated branches in both the positive and negative field regions. The intercepts of these fits are averaged to give the estimated saturation magnetization.

We identify two main sources of error in the VSM measurements: First, errors arise from fitting, particularly from the linear background subtraction required to differentiate the small ferrimagnetic response from the paramagnetic substrate contribution. This is estimated via the root-mean-square deviation of our fit. We evaluate this for both saturation regimes at positive and negative fields and take the maximum of the two. Second, errors arise from instrumental

4

noise and drift, which causes a change in the gradient between the positive and negative field regions. This is estimated via the standard deviation of the averaging for saturation magnetization. For TmIG and YIG films a custom-built VSM with improved sensitivity and noise-to-signal ratio was used, resulting in smaller error bars than for the EuIG data.

Supplementary Note 2*: Spin Hall magnetoresistance: Fitting*
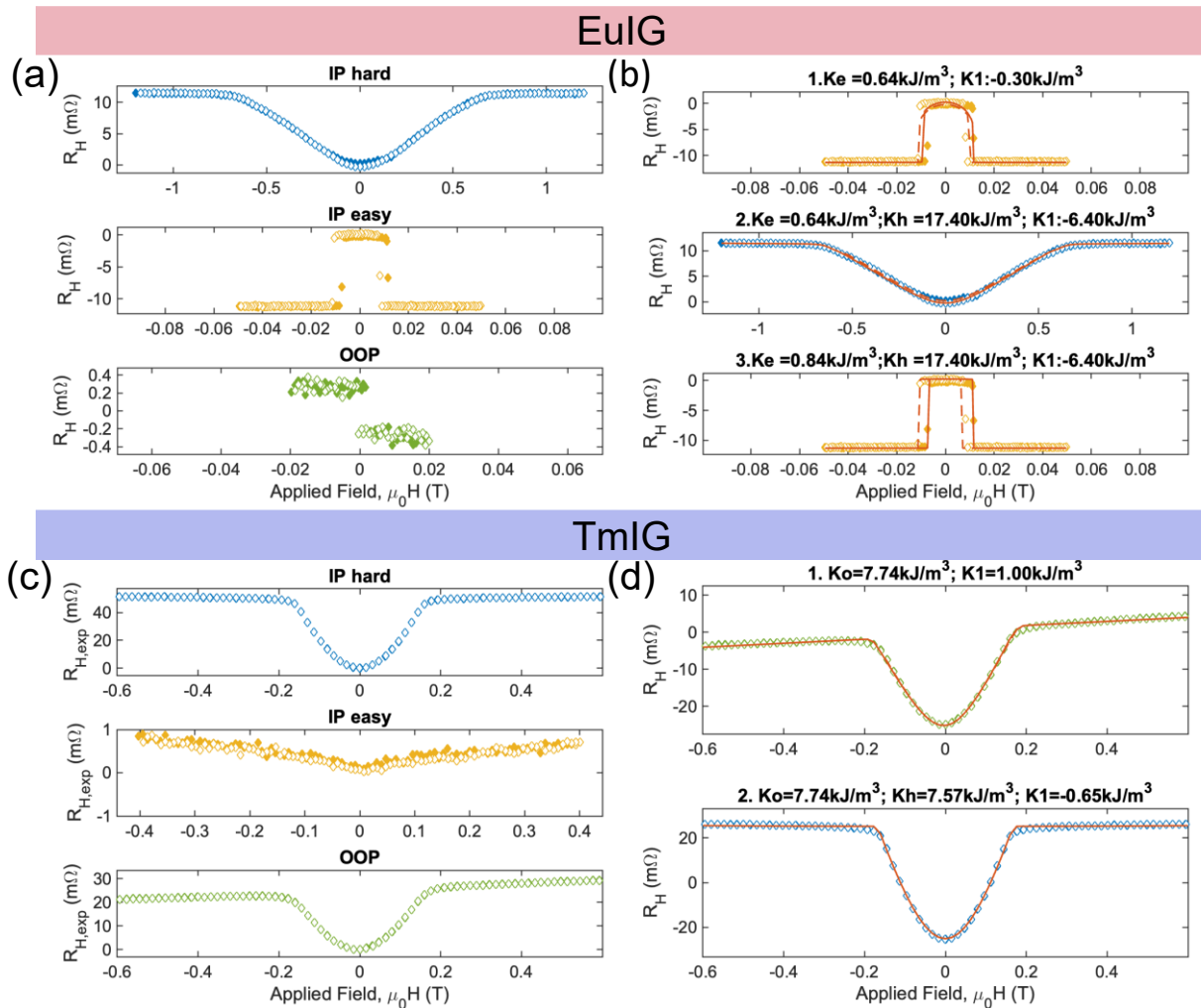
Fig. S2. Spin-Hall magnetoresistance experimental data and fitted results for EuIG/GGG(110) (top) and TmIG/GGG(110) (bottom). (a), (c) Measurements with the field applied along the in-plane hard, in-plane easy, and out-of-plane directions. For EuIG/GGG(110), the three panels in

(b) represent fitting results from steps 2 to 4 in the fitting protocol, where the fitting improved from the top panel to the bottom panel when the manual switching is implemented. For TmIG/GGG(110), the last step 4 is not necessary, as the fits shown in (d) are accurate.

Spin Hall magnetoresistance measurements are numerically fitted using a macrospin model by minimizing the mean squared error between the resistance value evaluated using a macrospin model and the value obtained from experimental measurements for all applied field values [40]. In the macrospin model, the equilibrium magnetization direction was determined by minimizing the total energy in Eq. S3. with respect to θ and ϕ, where E_A is the total anisotropy energy consisting of a two-fold symmetric term (magnetoelastic and magnetostatic) and a cubic symmetric term, $E_{\mathrm{MC}}(\theta, \phi)$ (magnetocrystalline) with the magnitude given by the anisotropy constant K_1 in Eq. S4. θ_H and ϕ_H are the polar and azimuthal angles for the applied field direction with respect to the coordinate system defined by $\boldsymbol{a_1} = [\bar{1}10]$, $\boldsymbol{a_2} = [001]$ and $\boldsymbol{a_3} = [110]$.

$$E_{tot} = E_A(\theta, \phi) + \mu_0 \vec{M} \cdot \vec{H}$$

$$= E_A(\theta, \phi) + \mu_0 M_s H (\cos \phi \sin \theta \cos \phi_H \sin \theta_H + \sin \phi \sin \theta \sin \phi_H \sin \theta_H + \cos \phi \cos \theta_H) \quad (S3)$$

$$E_A(\theta, \phi) = E_{\mathrm{MC}}(\theta, \phi) + (E_1 + E_2 \cos^2 \phi) \sin^2 \theta,$$

$$E_{\mathrm{MC}}(\theta, \phi) = K_1 \left(\frac{\cos^4 \theta}{4} - \frac{\cos^2 \theta \sin^2 \theta \cos^2 \phi}{2} + \frac{\cos^4 \phi \sin^4 \theta}{4} + \cos^2 \theta \sin^2 \theta \sin^2 \phi + \cos^2 \phi \sin^2 \phi \sin^4 \theta \right)$$

The equilibrium magnetization vector is then converted to resistance with Eq. S5, where $\phi_I = 45°$.

$$R_{\mathrm{H}} = R_{\mathrm{SMR,AHE}} \cos \theta + R_{\mathrm{SMR}} \sin^2 \theta \sin 2(\phi - \phi_I) + R_{\mathrm{OHE}} \mu_0 H_3 \qquad (S5)$$

Additional steps in the fitting protocol for EuIG:

1. Since thermally activated switching occurs due to a non-negligible magnetocrystalline anisotropy, fitting to the intermediate axis gives a lower K_1 and a slightly smaller K_{OOP} than the actual value. Additional steps have been added to the fitting protocol to improve fitting accuracy.

6

2. Coupled fitting to extract magnetoresistance coefficients. A linear fit was made to the two saturated regions in the field sweep along a_3 to extract the average of gradients as R_{OHE}. A linear fit to the two saturated regions in the field sweep along a_3 was made, yielding the difference between the intercepts of two fits as $R_{\text{SMR,AHE}}$, and the average of intercepts as the offset. $R_{\text{SMR,AHE}}$ was obtained from the opening of a_1 and a_2 at zero field and the average at zero field as the offset. The Hanle effect correction with the first order approximation of $R_{SMR} = R_{offset} + R_{SMR,0}(1 + (\mu_0 H/D)^2)$ was made by fitting to high field values of field sweep along a_2. $R_{SMR} + R_{offset}$ was extracted from the saturated regions of field sweep along a_2. R_{SMR} was determined from the average.

3. The Hall coefficients were fixes and a fit to the field sweep along the intermediate axis was made to obtain initial values for $K_{OOP} = K_e = E_1 - E_2$ and K_1 values.

4. A fit to the hard axis with fixed K_{OOP} yielded accurate K_1 and $K_{IP} = K_h - 1/4K_1 = -E_1 - 1/4K_1$.

5. A refit to the intermediate axis with fixed K_1 and K_{IP} and manual input of switching field was used to extract K_{OOP}. When the switching field is reached, the solution to the equilibrium magnetization is switched to global minimum instead of the local minimum (which was used previously to simulate the hysteresis behaviour).

Fig. S2 shows the experimental data in (a) for EuIG and (c) for TmIG and the fitted results in (b) for EuIG and (d) for TmIG. The three panels in (b) represent fitting results from steps 2 to 4, where the fitting improved from the top panel to bottom panel when the manual input of the switching field was implemented. Improved agreement between fit and data is also achieved in the middle panel when magnetocrystalline anisotropy is introduced. Two panels in (d) represent fitting results from steps 2 to 3 since switching does not occur. In the case of TmIG $K_{OOP} = K_o - K_h$, $K_{IP} = -K_h$.

The error of the SMR measurements is estimated by considering the contributions from fitting and the precision of our measurement setup. The fitting error is evaluated via the root-mean-square deviation of the SMR fit. The gradient of the resistance associated with each field step gives an estimate of the experimental errors. The two error terms are considered cumulatively.

The initial error estimates in Ohms were converted into percentage errors then the anisotropy energies were calculated via normalization with the Planar Hall coefficient for each individual data point. The errors in the anisotropy energies do not include the propagating errors of the saturation magnetization and thickness measurements. An average percentage error is calculated to be $5.8 \pm 0.3\%$ from the TmIG dataset and an upper bound of 10% is used as the percentage error for EuIG because of the uncertainties associated with fitting to additional features associated with the magnetocrystalline anisotropy. We note that the fitting error contribution for the YIG (SI Note 5) is significantly larger than for EuIG and TmIG due to low field switching events not captured with our fitting protocol.

Supplementary Note 3*: Discussion of the effect of out-of-plane strain variation*
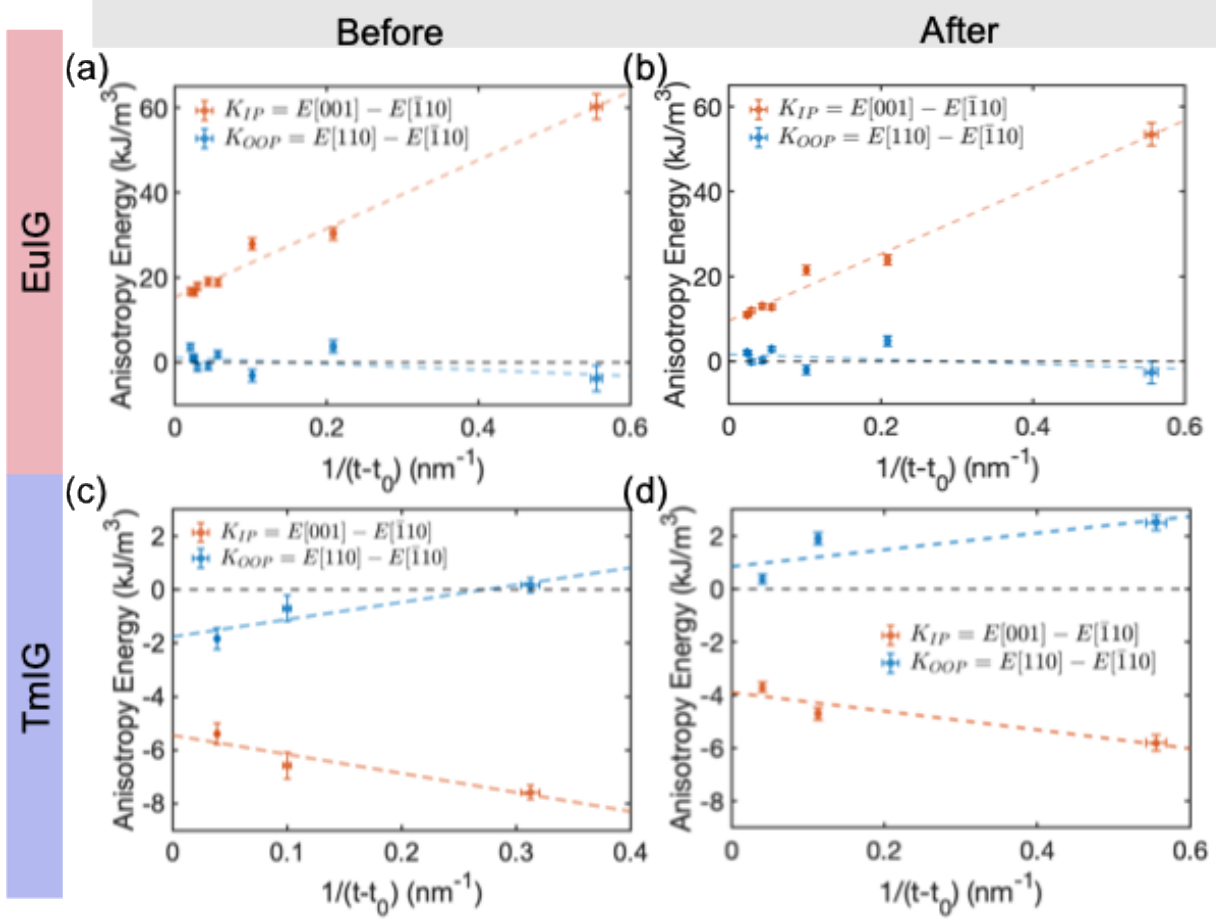
Fig. S3. Anisotropy energy plotted against film thickness before strain correction for (a) EuIG/GGG(110) and (b) TmIG/GGG(110) and after strain correction for (c) EuIG/GGG(110) and (d) TmIG/GGG(110).

The bulk magnetoelastic contribution to the magnetic anisotropy can be calculated from the measured strain state. The bulk magnetoelastic anisotropy $E_{ME}(\theta, \phi)$ can be written in Eq. S6, where α_i is the direction cosine between the magnetization vector $\boldsymbol{M}(\theta, \phi)$ and the principal crystallographic axes, $i, j \in [100], [010], [001]$, B_1 and B_2 are the magnetoelastic coefficients and $\boldsymbol{e}'$ is the strain tensor defined in principal crystallographic axes related to the strain tensor in film coordinate axes $\boldsymbol{e}$ in Eq. S7.

$$E_{ME}(\theta, \phi) = B_1 \sum_i \alpha_i^2(\theta, \phi) e'_{ii} + B_2 \sum_{i,j} \alpha_i(\theta, \phi) \alpha_j(\theta, \phi) e'_{ij} \qquad (S6)$$

$$e' = QeQ^T = \frac{e_0}{2}\begin{pmatrix} 1 + e_{33}/e_0 & -1 + e_{33}/e_0 & 0 \\ -1 + e_{33}/e_0 & 1 + e_{33}/e_0 & 0 \\ 0 & 0 & 1 \end{pmatrix}, \text{where } Q = \begin{pmatrix} -\frac{1}{\sqrt{2}} & 0 & \frac{1}{\sqrt{2}} \\ \frac{1}{\sqrt{2}} & 0 & \frac{1}{\sqrt{2}} \\ 0 & 1 & 0 \end{pmatrix} \quad (S7)$$

The bulk magnetoelastic contribution to in-plane and out-of-plane anisotropy can then be calculated as

$$K_{IP,ME} = E_{ME}[001] - E_{ME}[\bar{1}10] = (e_0 - e_{33})\left(\frac{1}{2}B_1 - \frac{1}{4}B_2\right) \quad (S8)$$

$$K_{OOP,ME} = E_{ME}[110] - E_{ME}[\bar{1}10] = -\frac{1}{2}(e_0 - e_{33})B_2 \quad (S9)$$

Small variations in e_{33} shown in Fig 2 (c) and (d) linearly propagate to the magnetoelastic contribution when making comparisons across samples. However, we show that the effect of these variations on the extracted bulk and surface anisotropy contributions are small and only add quantitative corrections to the results. We carry out the strain correction by performing an iterative fitting algorithm. We first subtract K_{OOP} by $K_{demag} = \frac{1}{2}\mu_0 M_s^2$ to obtain magnetoelastic contributions to experimentally measured effective anisotropy.

1. Initialize B_1 and B_2 using literature values.
2. Use Eq. S8 and Eq. S9 to calculate the magnetoelastic contribution to the bulk in-plane $K_{IP,Bulk}^{Eq}$ and out-of-plane anisotropy $K_{OOP,Bulk}^{Eq}$.
3. Perform strain correction by subtracting experimentally measured K_{IP} and K_{OOP} by a variation $dK_{IP,ME}$ and $dK_{OOP,ME}$ caused by strain variation de_{33} determined by Eq. S8 and Eq. S9.
4. Fit strain-corrected K_{IP} and K_{OOP} to obtain experimentally determined bulk in-plane $K_{IP,Bulk}^{Exp}$ and out-of-plane anisotropy $K_{OOP,Bulk}^{Exp}$. Calculate B_1 and B_2 using $K_{IP,Bulk}^{Exp}$ and $K_{OOP,Bulk}^{Exp}$ with Eq. S8 and Eq. S9 and update the values for B_1 and B_2.
5. Repeat steps 2 − 4 until the calculated bulk anisotropies and fitted bulk anisotropies converge (difference $< 0.001 kJ/m^3$).

Fig. S3 shows a comparison in the K vs 1/t plot before and after strain correction. We summarize the anisotropy values extracted before and after strain correction in Table. S1 and small changes are observed within the error bar. We conclude that the out-of-plane strain variation does not have a major impact on our anisotropy determination. We also compare the extracted B_1 and B_2 values before and after strain correction with literature values for bulk REIG in Table S2. A general agreement is observed.

|	Before Strain Correction				After Strain Correction			
	K_{IP}^{bulk} kJ/m^3	K_{OOP}^{bulk} kJ/m^3	$E_{IP}^{surface}$ $\mu J/m^2$	$E_{OOP}^{surface}$ $\mu J/m^2$	K_{IP}^{bulk} kJ/m^3	K_{OOP}^{bulk} kJ/m^3	$E_{IP}^{surface}$ $\mu J/m^2$	$E_{OOP}^{surface}$ $\mu J/m^2$
EuIG	15.3	1.1	80.8	−3.9	11.1	1.8	74.8	−6.2
TmIG	−5.4	−1.7	−3.7	3.4	−3.7	0.7	−6.4	6.0

Table S1. Fitted bulk and surface anisotropy energies before and after strain correction for EuIG and TmIG.

	This work, before strain correction 10^6 Pa		This work, after strain correction 10^6 Pa		Literature, bulk, 10^6 Pa [23]	
	B_1	B_2	B_1	B_2	B_1	B_2
EuIG	-1.88	-0.30	-1.36	-0.21	-5.07	-0.41
TmIG	-0.3	1.6	-0.21	1.1	-0.338	1.19

Table S2. Extracted magnetoelastic coefficients before and after strain correction for EuIG and TmIG.

Supplementary Note 4*: Temperature-dependent anisotropy and magnetization measurement*
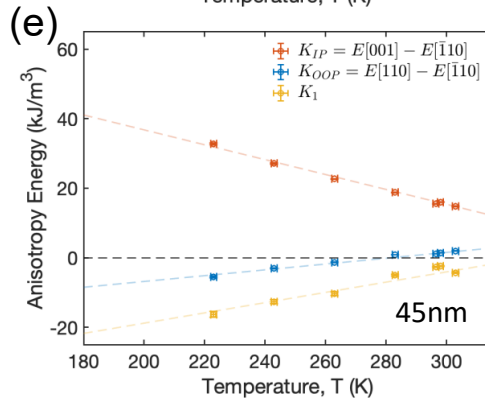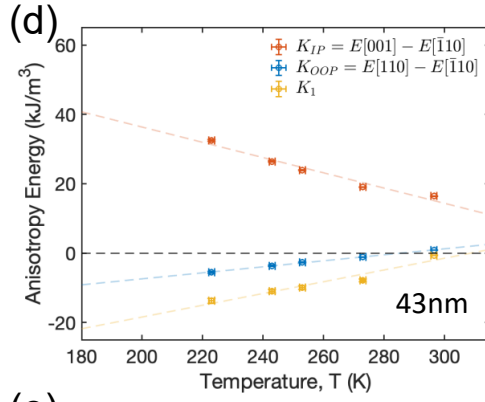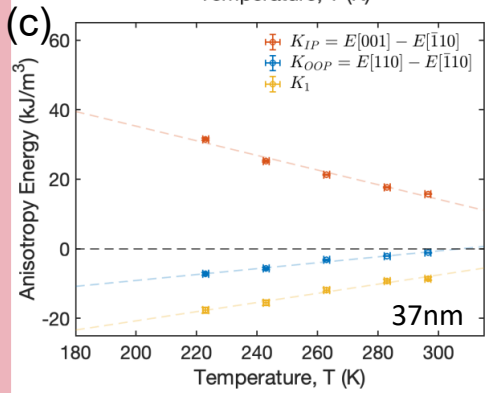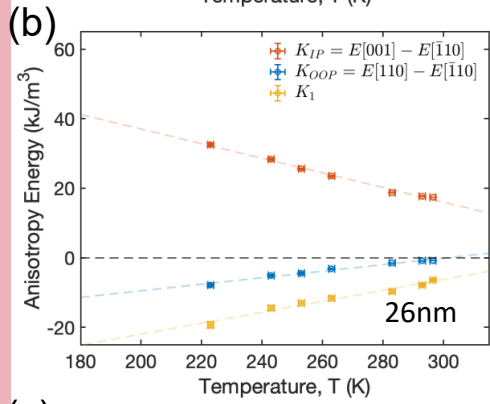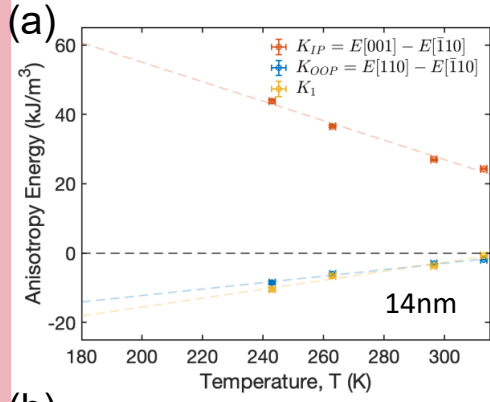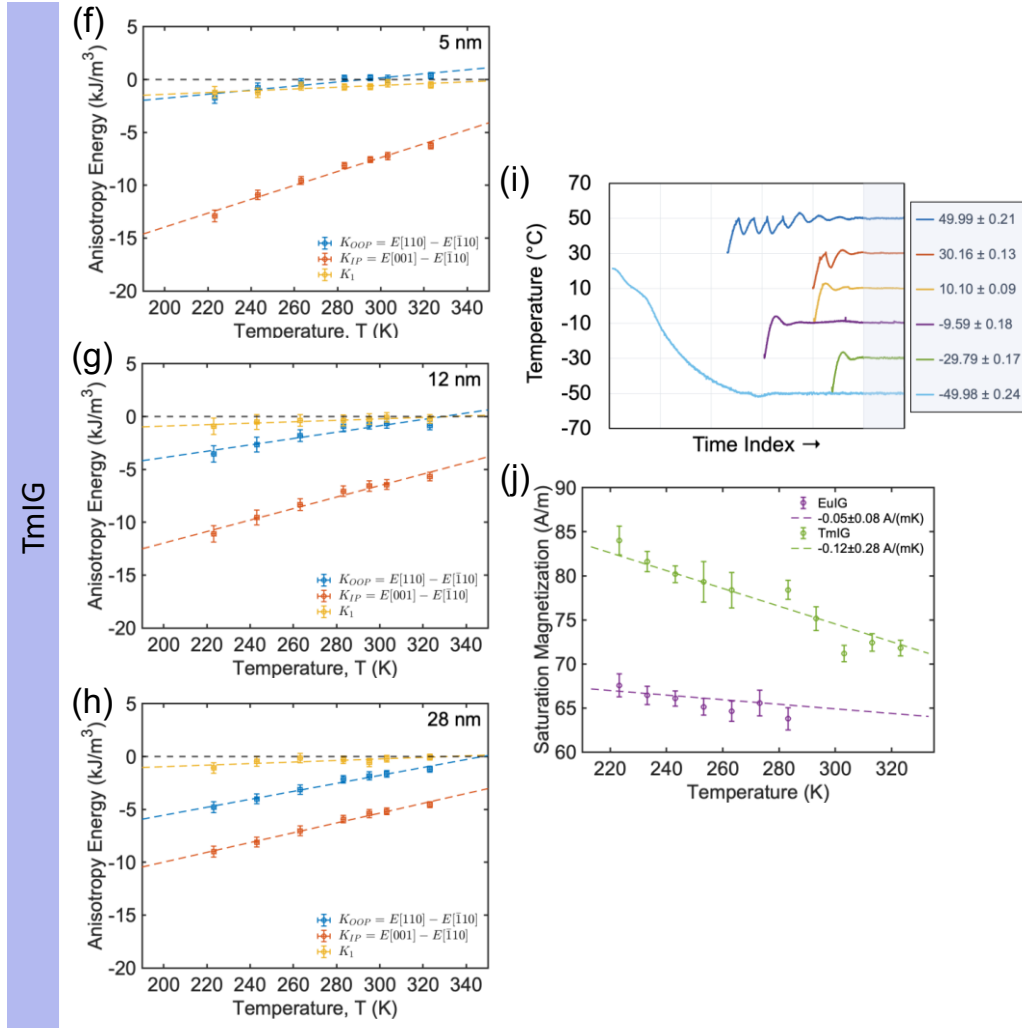
Fig. S4. Extracted anisotropy energies as a function of temperature (a) – (e) for EuIG/GGG(110) (t = 14nm, 26nm, 37nm, 43nm, 45nm), (f) – (h) for TmIG/GGG(110) (t = 5nm, 12nm, 28nm). (i) An example of the temperature stability during measurement. Data acquisition starts at the left bound of the shaded area. (j) The temperature dependence of the saturation magnetization for EuIG(45nm)/GGG(110) and TmIG(28nm)/GGG(110).

Temperature dependent spin Hall magnetoresistance measurements were performed on a home built cryogenic control system, where temperature of the sample is monitored via a thermocouple mounted on the sample holder. Typical temperature stability at different measurement temperatures is shown in Fig. S4 (i). Temperature variation of less than 0.5° is attained before the start of data acquisition. The in-plane and out-of-plane anisotropies are obtained from the field sweep of spin-Hall magnetoresistance measurements at each temperature, and their

temperature gradients $\Delta K_{IP}/\Delta T$ and $\Delta K_{OOP}/\Delta T$ are obtained from a linear fit of anisotropy values measured from 243K to 296.5K (r.t.) for thicknesses 13nm, 26nm, 37nm, 43nm, 45nm of EuIG and 5nm, 12nm, 28nm of TmIG. A complete set of extracted anisotropy energies at different temperatures and thicknesses is shown in Fig. S4 (a) – (e) for EuIG and Fig. S4 (f) – (h) for TmIG. The temperature dependence of surface and bulk in-plane and out-of-plane anisotropies can be obtained from a plot of temperature gradients against $1/(t - t_0)$. Clear easy-plane transitions (EPT) and hard-plane transitions (HPT) can be observed in EuIG and TmIG respectively as temperature changes from 223K to 323K.

The $M_{s,0}$ values used for anisotropy energy calculation in Supplementary Note 4 is obtained from temperature dependent vibrating sample magnetometry measurement shown in Fig. S4 (j). An offset can be introduced during temperature dependent VSM due to constraint on sample position imposed by heat furnace. Therefore, the gradient of the linear fit from temperature dependent VSM and the M_s measured at room temperature are used for $M_{s,0}$ extrapolation at a given temperature.

$$M_{s,0}(T) = M_{s,0}(296.5K) + gradient \times (T - 296.5)$$

***Supplementary Note 5***: *Additional thickness series data for yttrium iron garnet*
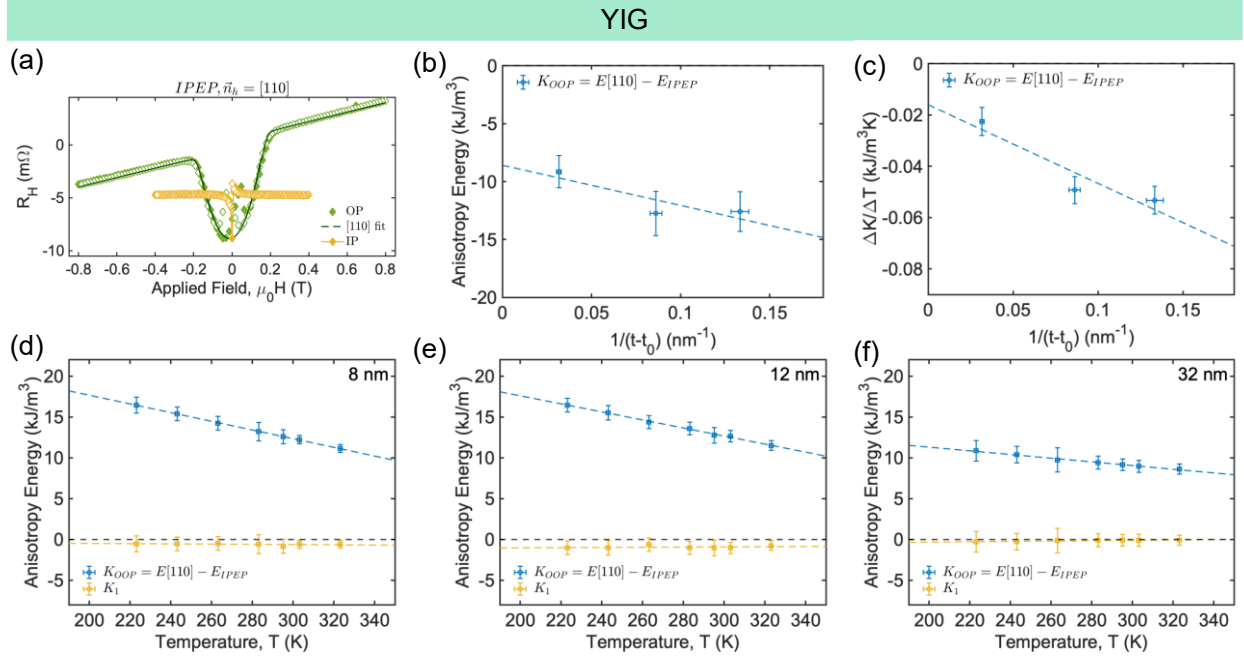
Fig. S5. Anisotropy characterization of YIG thickness series (t = 8, 12, 32 nm). (a) Example spin-Hall magnetoresistance measurement for Pt/YIG(32nm)/GGG(110) at $-10°C$ with field applied along an in-plane axis (yellow) with lowest energy and the out-of-plane axis (green). YIG shows an in-plane easy-plane configuration. We fit the out-of-plane measurement to extract the anisotropy energy for each film K_{OOP} = E [110] - E_{IPEP}. We suspect the low field artefacts to stem from the magnetocrystalline anisotropy. (b) The (room-temperature) out-of-plane anisotropy 1/t dependency shows the presence of a strong out-of-plane surface anisotropy in Pt/YIG/GGG. (c) Temperature dependence of the anisotropies ($\Delta K/\Delta T$). (d)-(f) Temperature dependent anisotropy measurements used for the extraction of (b) and (c). A monotonically decreasing trend is observed in the OOP anisotropy energies with increasing temperature.

As opposed to TmIG and EuIG, YIG shows negligible in-plane surface and bulk anisotropy since both spin-orbit coupling and lattice mismatch strain are negligible. An easy-plane anisotropy within the film plane is observed with some switching events which is attributed to a weak in-plane anisotropy [40]. Due to the negligible lattice mismatch strain ($a_{YIG} = a_{GGG} = 12.376 \, Å$) no out-of-plane surface anisotropy originating from Néel surface anisotropy is expected and as discussed, the out-of-plane surface anisotropy comes solely from Rashba SOC. The YIG thickness series (t = 8, 12, 32 nm) was hence used as a control series. The general measurement protocols for XRD, XRR, VSM and SMR measurements remained the same as for TmIG and

EuIG. We extracted a dead layer thickness of 0.8 nm and $M_{s,0} = 108 \pm 1 kA/m$. SMR measurements are performed with field applied along a direction within the film plane (IP) and out-of-plane (OP). Typical SMR curves are shown in Fig S5 (a). From the in-plane SMR curve, we observe that the in-plane anisotropies are negligible for all films and are therefore reported as zero with an error bar corresponding to the magnetocrystalline anisotropy which is the dominant contribution to in-plane anisotropy in YIG. At low fields, switching artefacts were observed. We attribute these to potential contributions from the magnetocrystalline anisotropy, which was not considered for the alignment of the patterned devices. Effect of magnetocrystalline anisotropy on switching behavior was discussed in our previous work [40]. We extract the anisotropies by fitting to datapoints above the switching field, which gives accurate anisotropy values. The anisotropy energy density is plotted against 1/t (Fig. S5 (b)) from which we extract the surface and bulk anisotropy contributions. The temperature dependence of bulk and surface anisotropies are extracted from the $\Delta K/\Delta T$ against 1/t plot (ΔT = 320K-220K) in Fig. S5 (c). The complete data set for extracted anisotropy energy density as a function of temperature is shown in Fig. S5 (d) – (f).

Supplementary Note 6*: Density functional theory calculation for surface energies*
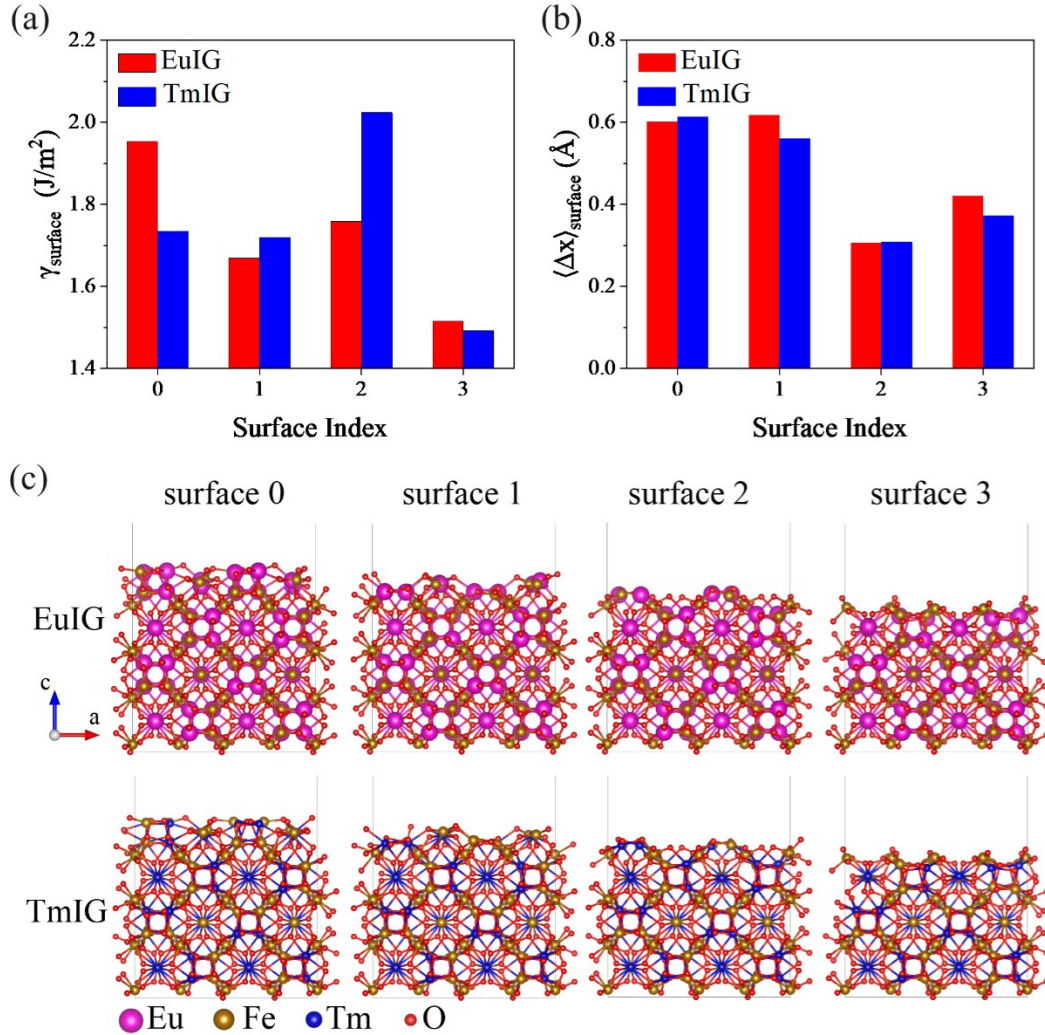
Fig. S6. (a) Surface energy density γ_{surface}, (b) average surface ionic displacement, and (c) atomic structure of different possible termination of the EuIG and TmIG (110) surface. The four possible terminations of the surfaces are indexed as surface 0, 1, 2, and 3. Panel (b) indicates evident ionic displacements during surface relaxation of all surfaces. In panel (c), the first and second row show the surface of EuIG and TmIG, respectively, and each column shows one surface termination.

The atomic configuration and surface energy of the EuIG and TmIG [110] surfaces are calculated by spin-unrestricted density functional theory (DFT) [53]. According to the arrangements of Eu and Fe [110] atomic planes, four inequivalent surface terminations are identified, as shown in Fig. S6 (b). We construct the initial atomic configurations of each surface by terminating the REIG bulk configuration at a given RE/Fe [110] atomic plane (with strain

determined in our experiments) and include adjacent oxygen atoms so that the charge state is balanced. Namely, we classify a set of oxygens into each RE/Fe [110] plane so that every RE/Fe [110] atomic plane has a chemical formula $RE_xFe_yO_{3(x+y)/2}$. In the calculation, the surface is simulated as a slab of REIG with a vacuum layer of 10 Å. The bottom of the slab is always set as surface 3 in all configurations, while the top surface goes through all possible terminations. Then, the relaxed atomic structures and total energies of the surfaces are calculated from the constructed initial configurations.

In order to calculate the electronic energy, the projector-augmented wave (PAW) method [54] is implemented by Vienna ab initio Simulation Package (VASP) [55] with a cut-off energy of 400 eV. Electron exchange-correlation interaction is evaluated using the generalized gradient approximation (GGA) by the Perdew-Burke-Ernzerhof (PBE) functional [56]. The k-point mesh is generated by the Monkhorst-Pack method [57] with a separation of 0.4 rad/Å. For supercell size larger than 12 Å, the k-point is set Γ-only. In all calculated surfaces, the electronic iteration energy was converged to 10^{-5} eV, and forces on all atoms due to ionic relaxation converged below 0.05 eV/Å.

The DFT calculations provide total energy E_i^S of the slab i ($i = 0, 1, 2, 3$), whose compositions are denoted as $RE_{2x_i}Fe_{2y_i}O_{3(x_i+y_i)}$. Here, x_i and y_i are one half of the number of RE and Fe in the slab, respectively. Together with reference energies $E_{RE_3Fe_5O_{12}}$, $E_{Fe_2O_3}$, and E_{REO_3} of bulk REIG and oxides, we get the surface energy density γ_i of surface i as follow:

$$(\gamma_i + \gamma_3)A = E_i^S - x_i\mu_{RE_2O_3} - y_i\mu_{Fe_2O_3}, (i = 0,1,2,3) \qquad (SI10)$$

where we set $\mu_{RE_2O_3} = E_{RE_2O_3} + \delta$, $\mu_{Fe_2O_3} = E_{Fe_2O_3} + \delta$, $\delta = \frac{2E_{Re_3Fe_5O_{12}} - 3E_{Re_2O_3} - 5E_{Fe_2O_3}}{8}$, and A is the area of the [110] surface in one unit cell. This setting satisfies $2E_{RE_3Fe_5O_{12}} - 3E_{RE_2O_3} - 5E_{Fe_2O_3} = 0$, which means a bulk REIG gives zero grand thermodynamic potential $E_{bulk} - x_{bulk}\mu_{RE_2O_3} - y_{bulk}\mu_{Fe_2O_3}$ in the right-hand side of Eq. S10, so the grand thermodynamic potential of the slab equals the summation of surface energies on both sides. Surface energy densities $\gamma_{0,1,2,3}$ are then determined by solving the four equations in Eq. S10, as shown in Fig. S6 (a).

The surface energy density of surface 3 is the smallest within the four surfaces for both EuIG and TmIG. Therefore, the surface 3 with Fe-layer termination is thermodynamically favorable. This can be explained as only surface 3 has a pure Fe termination with no RE atoms in the top layer. As the RE-O bond has a higher bond energy than the Fe-O bond, surface 3 breaks only Fe-O bonds without breaking RE-O bonds, so its surface energy is lower. We notice that γ_3 is at least 154 mJ/m^3, about two times the surface energy density of water, indicating a strong thermodynamic driving force towards surface 3 structure. This leads to a high probability to obtain the same surface termination among different samples, which gives consistent surface magnetic anisotropy.

Prior work confirms that rare-earth iron garnet thin films grown by pulsed laser deposition on GGG (110) orientation adapt a layer-by-layer growth [51], where RHEED oscillations with a period corresponding to ¼ unit cell were observed. In Fig. S7 (b), the four surface types also appear with the same period of ¼ unit cell, which aligns with the RHEED oscillation period. This is consistent with film growth occurring through the nucleation and propagation of a single surface termination instead of mixed surfaces. In the case of a mixed surface termination, since all four possible surface terminations show a two-fold symmetry, it will still contribute to both an IP and OOP surface anisotropy, but with different strengths. Therefore, in the unlikely event of a mixed surface termination, there will be quantitative corrections to the IP and OOP surface anisotropy values, but the qualitative trend will not be affected.

Supplementary Note 7*: Magnetic domain structure*
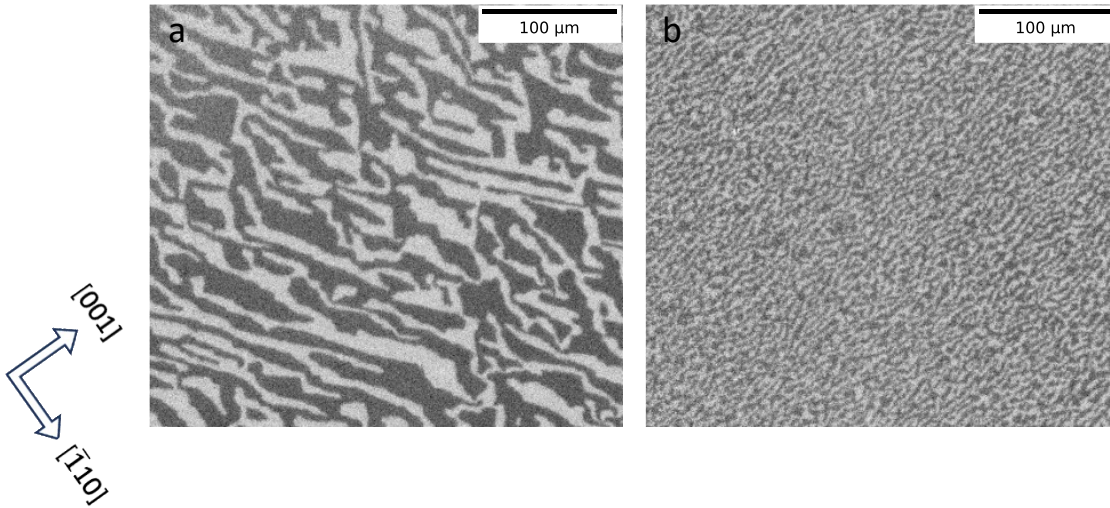
Fig. S7. Magnetic domain structures after field demagnetization for (a) Pt(1.5nm)/EuIG(26nm)/GGG(110) and (b) Pt(1.5nm)/EuIG(37nm)/GGG(110).

Studying the magnetic domain structures is interesting in systems with complex anisotropy landscapes on the low symmetry (110) substrate orientation. Using a polar magneto-optical Kerr effect (MOKE) microscope, we obtained differential MOKE images for the magnetic domain structures after a demagnetization field sequence shown in Fig. S7. The magnetic domains for a 26nm and a 37nm EuIG on GGG(110) substrate are shown in Fig. S8 (a) and (b), respectively. For both thicknesses, stripe domains are observed due to the presence of an in-plane anisotropy which lifts the degeneracy between domain walls along different crystallographic orientations. The length of the stripe domains appears aligned along the [001] high energy axis in the 37nm film, which gives rise to a high density of Néel domain walls. However, the stripe domains are aligned 45 degrees from the [001] and [$\bar{1}$10] directions in the 26nm film, which gives the domain walls a mixed character, likely due to the high domain wall energies in Néel domain walls of extended length. The average domain size is much larger in the 26nm film than in the 37nm film, because both the IP and the OOP anisotropy are larger in the 26nm film which increases the energy cost for domain wall formation.

Supplementary Note 8*: Atomic Force Microscopy*
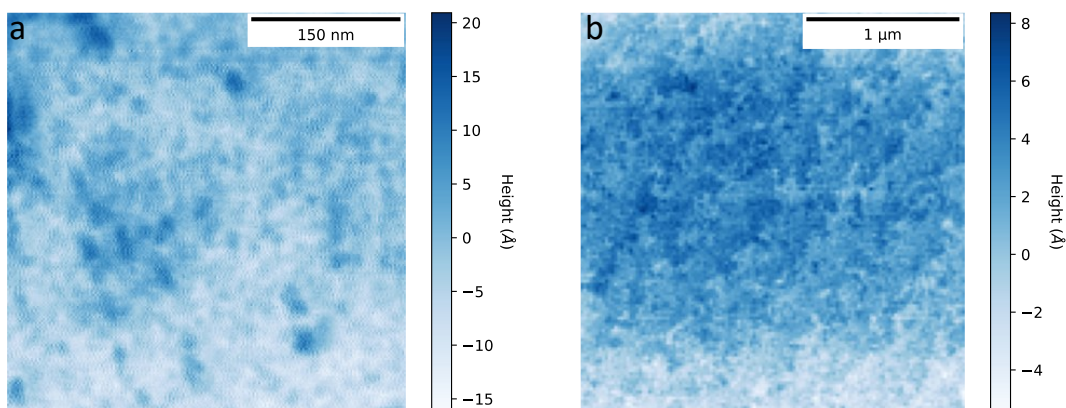
Fig. S8. AFM scans for (a) EuIG(10 nm)/GGG(110) and (b) EuIG(43 nm)/GGG(110).

Atomic force microscopy (AFM) is performed on the garnet films before Pt deposition as shown in Fig. S8. Examples of AFM scans are shown for EuIG(10 nm)/GGG(110) in Fig. S8a and EuIG(43 nm)/GGG(110) in Fig. S8b. The roughness (standard deviation) is measured to be 4 Å for the 10 nm film and 2 Å for the 43 nm film, demonstrating a consistent surface quality across the thickness range.